THESIS

THE CHANGING NATURE OF CONVECTION OVER EARTH'S TROPICAL OCEANS FROM A WATER BUDGET PERSPECTIVE

Submitted by

Nicolas Leitmann-Niimi

Department of Atmospheric Science

In partial fulfillment of the requirements

For the Degree of Master of Science

Colorado State University

Fort Collins, Colorado

Spring 2023

Master's Committee:

Advisor: Christian Kummerow

Eric Maloney
Mazdak Arabi

Copyright by Nicolas Leitmann-Niimi 2023

All Rights Reserved

ABSTRACT

THE CHANGING NATURE OF CONVECTION OVER EARTH'S TROPICAL OCEANS FROM A WATER BUDGET PERSPECTIVE

Consistent spatiotemporal hydrologic measurements over Earth's oceans are only feasible with satellite remote sensing. The water budget components of an atmospheric column are precipitation (P), evaporation (E) and horizontal water vapor divergence (divQ). Physically, the sum of these components leaves a residual term: the amount of water vapor stored inside the atmospheric column. When time series of the water budget components are made using independent data products, this residual term is unphysical, which must be a result of measurement error in one or more of the water variables. This study finds that variations in lack of closure are not random, and seeks to reveal underlying sources for long-term, high amplitude trends so that errors in observations may be better understood as the climate system evolves and assumptions built into the algorithms today may bias results into the future. Trends in the residual are particularly significant over the Tropical West Pacific (TWP), Southern Tropical East Indian (STEI) and Tropical Central Pacific (TCP), where there are multi-year residual trends that maintain a consistent magnitude of 1 mm/day. While there are still residual discrepancies over the Tropical Western Indian (TWI), Tropical Eastern Pacific (TEP) and Tropical Atlantic Ocean (TAO), closure is overall better, as residual trends are more annual in variation and less unphysical in magnitude.

This study hypothesizes that the first-order explanation for potential long-term biases lies in shifting convective organization. Convective organization changes are quantified using the amount of rain explained by three different regimes of convection (shallow, deep isolated and deep organized), which are dubbed convective rain states (CRS). A second-order explanation lies in relative ice amount. Relative ice amount is represented by ice-rain ratio (IRR), the amount of ice per amount of rain present in the atmospheric volume as determined from spaceborne radars. Changes in CRS can cause biases because rainfall spatial correlations related to well-known errors (e.g. beam-filling, convective/stratiform microphysics) are likely responsible for over-and underestimation of precipitation, while changes in the relative ice amount in individual convective rain states can cause the precipitation to be under or over-estimated due to scattering effects. Over the TCP these changes are purely dictated by the El-Nino Southern Oscillation (ENSO), with organization becoming a clear function of SST. Over the STEI there is a circulation that stems from the Indian Ocean Dipole (IOD), leading to a CRS and IRR dependence on vertical wind shear. Finally, over the TWP, CRS is neither a simple function of SST nor shear, but rather seems to arise from a deeper ocean change of state: a coupling/decoupling of west Pacific SST with central and east Pacific SSTs that coincides with the global warming hiatus period. Two different mechanisms may be at play when it comes to shifts in convective organization during this period. Outside of 2001-2007, the regular mechanism sees low-level shear directing convective organization. During 2001-2007, TWP SSTs are much warmer than surrounding SSTs, leading to an anomalous mechanism that sees water vapor convergence and atmospheric instability favoring isolated convection.

The purpose of this study is not to locate specific algorithm retrieval or model deficiencies, but rather to connect long-term measurement errors with fundamental changes in dynamic characteristics of ocean environments. While these proposed mechanisms would explain much of the observed biases, this study cannot address quantitative biases, as these

depend on algorithm details and vary from one algorithm to another – although the qualitative trends are consistent among them.

ACKNOWLEDGEMENTS

Thank you, Chris Kummerow, for all you have taught me. Through your guidance in this project, you have helped me discern my own capabilities and passions, as well as my limits. Thank you for giving me the independence to think on my own while also keeping your door open every time I couldn’t. The glimpse you have given me into your problem-solving thought process and story-telling capabilities has shaped me as a scientist and researcher. I would also like to thank everyone in the group. In particular, Paula Brown and Eric Goldenstern, you both gave me so much of your time, and I hope to one day return the favor. Additionally, I would like to thank WeiTing Hsiao for the extensive fruitful conversations we shared during our collaborative efforts. Finally, I would like to thank Eric Maloney and Mazdak Arabi for taking the time to serve on my M.S. committee, as well as the NASA Energy and Water Study (NEWS) for funding my course of study.

I would like to mention my parents, JR, Lulu and Sasha for their love and support always. I learned 90% of everything I know about writing and editing from Mama. I have many friends to thank for getting me here, but I would especially like to highlight Claire, Dylan, Mira and Michael for an uncountable number of hours spent talking, laughing, crying and cooking together during my unforgettable time in Fort Collins, Colorado.

TABLE OF CONTENTS

CHAPTER 1: INTRODUCTION

The global hydrologic cycle acts to rectify energy imbalances dictated by the Earth's radiation budget. Radiation from the sun largely penetrates the atmosphere and is absorbed at the surface, causing an energetic imbalance between the upper and lower layers of the atmosphere. Water rectifies this imbalance by removing excess surface energy in the form of latent heat through evaporation, subsequently releasing it into the atmosphere through cloud condensation.

There are significant disagreements in the contribution of water to the global energy budget. The 80 W/m^2 global average latent heat flux in the energetic budget proposed by Trenberth et al. (2009) stands in contrast to the 88 W/m^2 suggested by Stephens et al. (2012), while the most recent global estimate from L'Ecuyer et al. (2015) is 81 W/m^2. There is a 10% uncertainty between these estimates, with differences primarily stemming from the different sets of observations each study had available at the time, as well as different decisions and priorities regarding the relationships between these observations. While the advances in quantifying a global energy budget have been remarkable, this uncertainty in latent heat fluxes is significant, especially as it easily eclipses the magnitude of climate change where it has been estimated that the Earth is warming at approximately 0.5 W/m^2 (IPCC 2021).

From a global perspective, strides have been made in understanding the effect that a warming climate will have on the dynamic distribution of water. The Clausius-Clapeyron relationship dictates that water vapor in the atmosphere increases by 7% for every 1 K warming of the atmosphere. While water vapor plays a central role in producing precipitation, it does not constrain it. Local precipitation and evaporation rates are impacted largely by dynamic variables like convective instability and water vapor convergence, both of which will also be impacted by system warming. Held and Soden (2006) confirmed this by conducting model experiments that showed that the precipitation and evaporation sensitivity to an increase in lower-tropospheric water vapor is muted to around 2-3% / K. This increase will not be globally uniform however, and it raises the question of what regional responses will be to a warming climate.

Any large-scale study of water budget components necessitates the use of remote sensing data as rain gauges are nearly non-existent over the oceans. Unfortunately, by virtue of being remotely sensed, none of these components are measured directly. In the past decade, as remote sensing datasets pertaining to the global water budget have matured, increasing in quality and temporal scale, studies that assess the quality and biases of these measurements on global scales have had to rely on inter-product differences (Adler et al. 2012) and water budget closure. Primarily, the concept of long-term regional water budget closure –how well estimates of water budget components sum to zero–is a succinct tool that uses discrepancies between measurements and physical truth to identify specific errors and areas of interest. Since the first atmospheric closure attempt of Dines (1917), all water and energy budgets have used closure to ensure that terms balance and provide estimates for terms like sensible heating that prove difficult to measure.

The general description of a regional water budget over an atmospheric ocean area (Peixoto and Oort 1992) can be expressed as follows:

$$\frac{\partial W}{\partial t} + \frac{1}{g}\int_0^{p_0} q(\nabla \cdot v)_H \, dp = E - P \qquad (1)$$

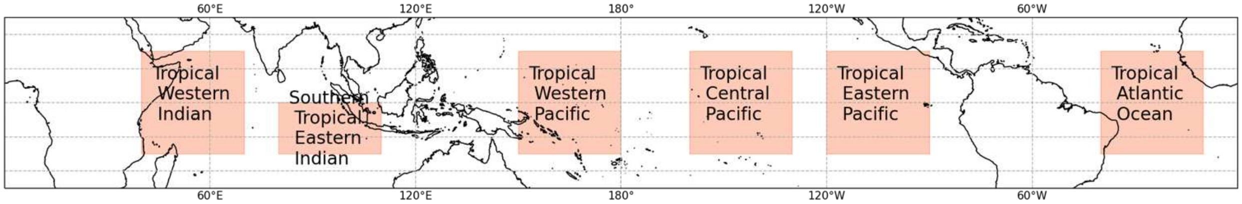

Figure 1: The physical locations of the six ocean 'basins' for this study.

The first term on the left-hand side is a water vapor storage tendency, the second term is the horizontal water vapor flux divergence integrated on all pressure levels. This is the atmospheric moisture transport term, and for convenience will be called divQ. On the right-hand side we have a representation of freshwater flux, the difference between evaporation into the atmospheric volume and the precipitation out of it. This study focuses on large-scale climatological trends, for which the water vapor storage term is negligible in comparison to the magnitudes of the remaining terms (Schlosser and Houser 2007). With this assumption, we can move all the terms to the left-hand side to arrive at our simplified water budget closure framework:

$$divQ + P - E \cong 0 \tag{2}$$

This framework is useful because it is a simple physical truth based on the law of mass conservation. If the datasets that measure these values do not close, then the data does not reflect physical truth. By taking independent products that measure these three values and combining them, this closure framework is a convenient metric to leverage products against each other, revealing errors that would otherwise be difficult to detect by just analyzing each dataset individually. This is especially true at regional scales where errors from local environmental factors may not average out as simple random errors. The crux of this study lies in errors that change in time. While overall biases exist and may be attributed to any of the products, changes in time are more subtle and likely represent physical changes in the system.

Many prior studies of closure have been static measures of water (L'Ecuyer et al. 2015; Rodell et al. 2015) and energy (Dines 1917; Trenberth et al. 2009) budgets, but now that satellite data spans climatological temporal scales, time series analyses of closure sheds light on changes in the hydrologic cycle. Brown and Kummerow (2014) conducted a narrower study of the closure of regional water budgets, focusing on the time series of correspondence of freshwater flux, (E-P), with divQ over five tropical ocean regions from 1998-2008. In this study, we examine almost the same regions with one exception: the Tropical Indian Ocean basin from Brown and Kummerow was split into two basins, the Tropical Western Indian (TWI) and Southern Tropical Eastern Indian (STEI), in order to isolate effects of the Indian Ocean Dipole (IOD) (Fig. 1). In this work, the tropical oceans were again picked to evaluate remote sensing products because they (a) contribute the largest amount to global rainfall, (b) are relatively homogeneous in both their surface and precipitation characteristics, and (c) showed markedly different trends among basins in Brown and Kummerow (2014). Brown and Kummerow's research was continued with work detailed in Koeritzer (2021). That work looked at closure using multiple data sources as input to the P, E and divQ components of the water budget, ultimately determining that the combination of the Precipitation from the Global Precipitation Climatology Project (GPCP; Adler et al. 2003), ocean Evaporation from SeaFlux (Roberts et al. 2010; Clayson et al. 2015), and divQ from ERA5 (Hersbach et al. 2020) leads to the most consistent water budgets across tropical ocean basins. Additionally, that effort discovered long-term trends in regional non-closure budgets that cannot be written off as random error. These trends vary on the order of years to decades (Fig. 2), and must come from specific physical biases in one or more of the data products, raising the question: what is changing in the hydrologic cycle to change the measurement bias in these water budget components?

Figure 2 displays the monthly and 12-month smoothed water balance residual term in each of the six tropical ocean basins. It is clear that the Southern Tropical East Indian (STEI), West Pacific (TWP), and Central Pacific (TCP) have the strongest multi-year to decadal trends in the residual. These basins reside in and near the Indo-Pacific warm pool, a high-SST area that see much more convective activity, precipitation, evaporation and horizontal convergence of water vapor than the other tropical ocean areas. Trends over the Tropical West Indian (TWI), Tropical East Pacific (TEP), and Tropical Atlantic Ocean (TAO) are largely annual and suggest that the products have high fidelity in these regions or at least do not suffer as much from large scale changes. This study aims to address the long-term trends in lack of closure, and therefore focuses on conditions over the STEI, TWP and TCP.

In order to gain insight into the nature of precipitating systems, this study utilizes precipitation and convective classification methods detailed in Elsaesser et al. (2010) and expanded upon by Henderson et al. (2017a and 2017b). The Tropical Rainfall Measuring Mission (TRMM; Kummerow et al. 1998) was a low-Earth orbiting satellite mission that monitored rainfall characteristics in the tropics and sub-tropics using passive microwave radiometers and active radar sensors. Elsaesser used the TRMM Precipitation Radar's (TRMMPR) retrievals of high-resolution reflectivity profiles, convective-stratiform pixel identification and instantaneous rain rates, deriving a k-means clustering scheme that classifies a 1x1° convective scene into different convective rain states (CRS): shallow, deep isolated (deepIso) or deep organized (deepOrg) convection. Right before its inevitable reentry into the

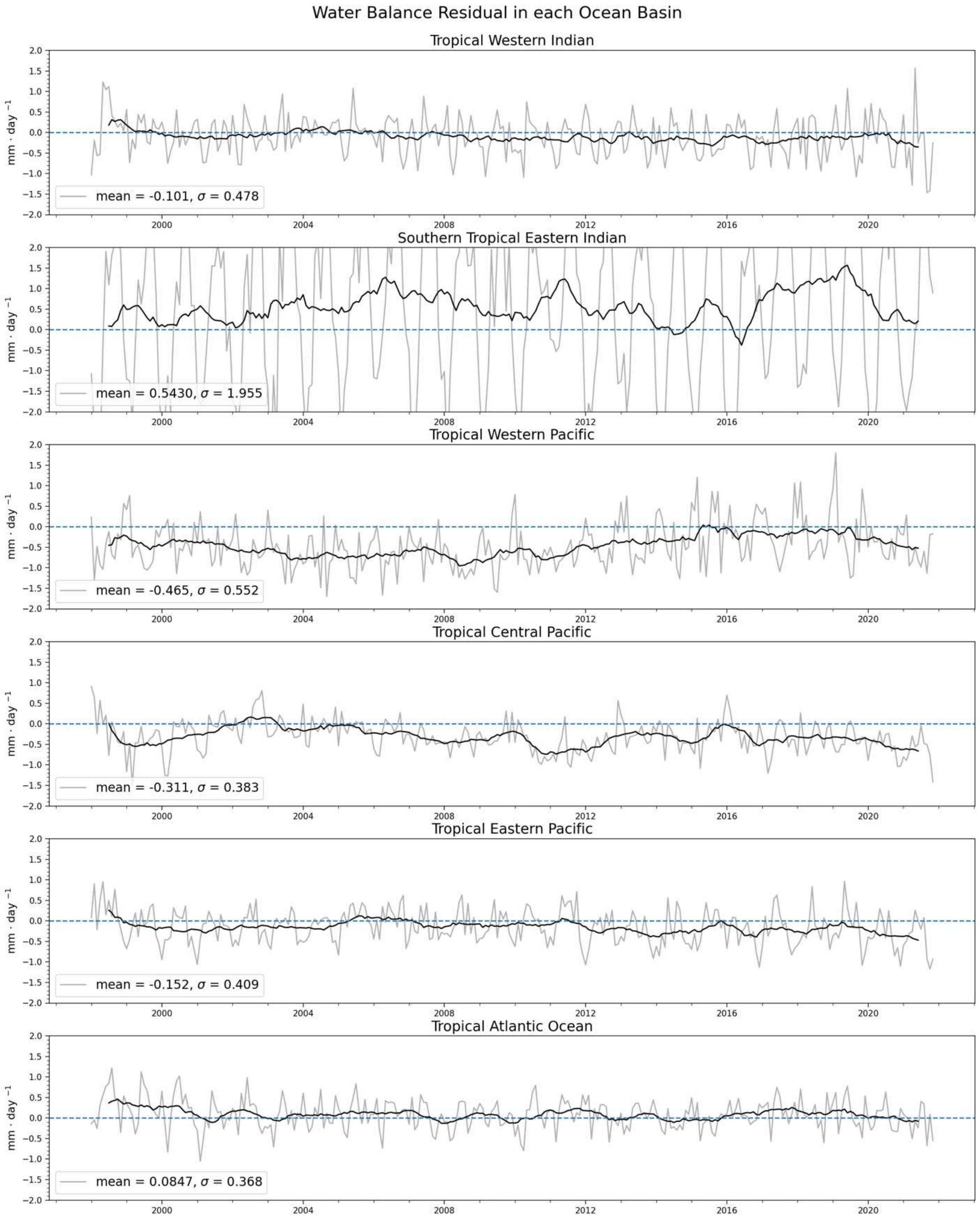

Figure 2: Monthly averaged divQ+P-E residual in light colors, with a 12-month smoothing filter applied in the darker colors. The STEI, TWP and TCP are the focus of this study because they have larger long-term trends in the water balance residual than the other basins.

atmosphere, TRMM's successor, the Global Precipitation Measurement Mission (GPM; Hou et al. 2014) launched in 2014, extending TRMM's rich data record and expanding its spatial regime to the higher latitudes. A significant portion of this study was dedicated to ensuring that Elsaesser's classification scheme was correctly applied to GPM's Ku-band Precipitation Radar (KuPR), an updated version of TRMMPR. This process of ensuring continuity across TRMM to GPM is detailed in Data section 2.4.

As will be shown, water budget imbalance in the six ocean basins is well correlated with long time-scale changes in convective organization that likely bias the underlying GPCP precipitation data product. Over oceans, the GPCP Version 2.3 Combined Precipitation Dataset used for this study relies on the Special Sensor Microwave Imager (SSMI) and Special Sensor Microwave Imager/Sounders (SSMIS) which are passive radiometers. Rain rates are derived from their relationship with brightness temperature, but this relationship is non-linear. Physically, microwave radiometers are hampered by having wide fields of view (FOV) that can average together non-uniform brightness temperatures (Tb) into a single measurement. If a FOV averages together more variable distributions of Tb than average, the non-linear relationship will lead to an incorrect output of rain-rate, a type of bias called the beam-filling effect (Wilheit et al. 1991; Graves 1993). An alternative bias mechanism relates to measurements of stratiform vs convective rain rates. Stratiform rain regions are statistically underrepresented in cloud model simulations, which have been found to convective biases in microwave precipitation retrievals (Kummerow et al. 2001). These are some possible mechanisms that explain why Henderson et al. (2017b) found that the TRMM Microwave Imager (TMI) can underestimate deep isolated convective rainfall by as much as 37%, and overestimate deep organized rainfall by as much as 33% when validated against the S-band radar located on the Kwajalein Atoll. One main hypothesis of this work is extending Henderson's results into a bias framework for tropical oceanic microwave retrievals: deep isolated CRS is underestimated while deep organized CRS is

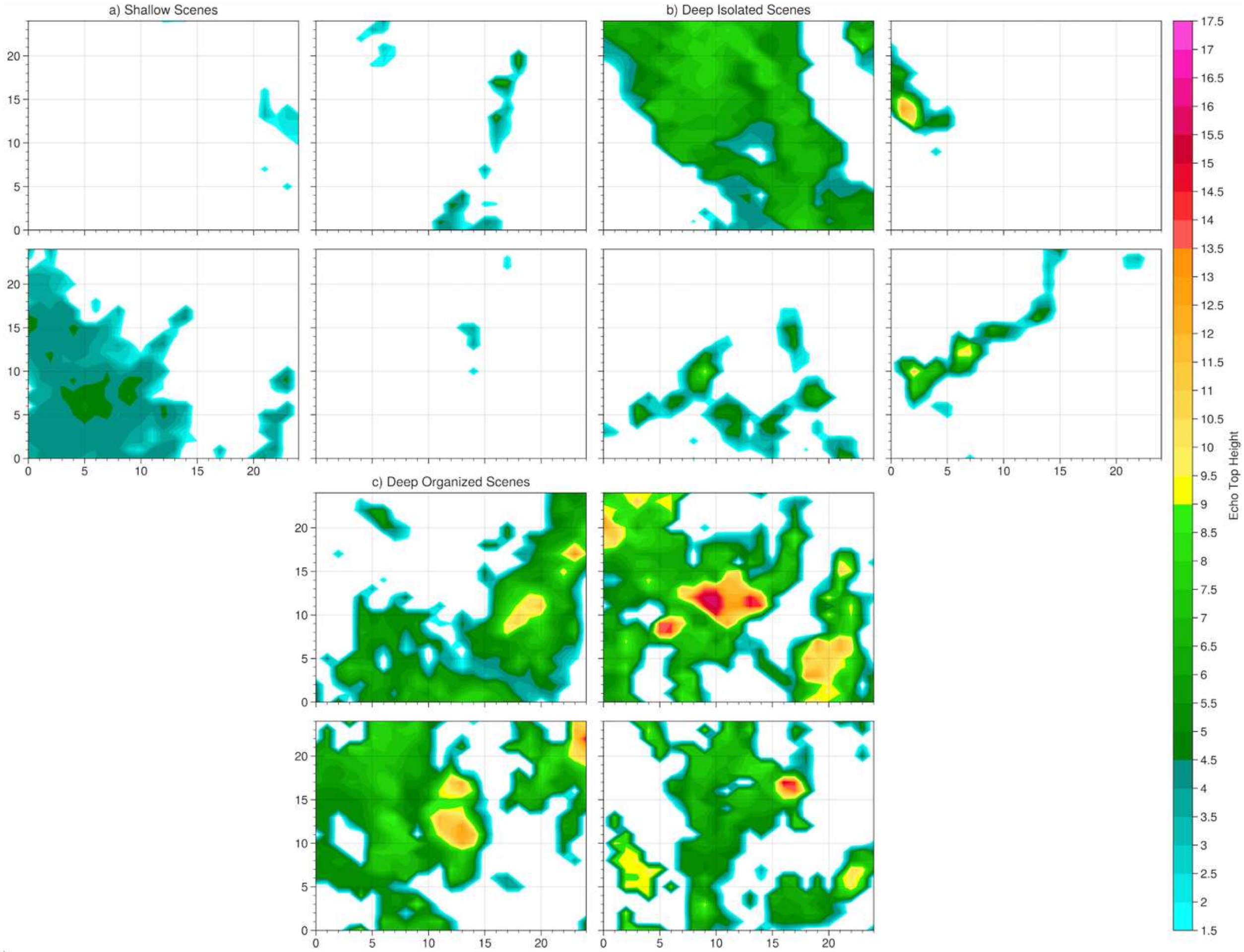

Figure 3: Echo Top Height (ETH) distribution examples of scenes classified into shallow, deep isolated and deep organized CRS

overestimated. Given the similarity in average echo structure between deep isolated and shallow CRS (Fig. 3), this framework will extend the bias framework hypothesis that shallow CRS is also underestimated.

The three CRS exemplified in Figure 3 share similar features across each basin but occur at different relative frequencies. The CRS sort convective scenes into conceptual categories, and a certain amount of rain is attributable to each of them. To give a clearer picture of the relationship between CRS and GPCP bias, this study uses the relative fraction of rainfall attributed to each CRS to evaluate and analyze convective organization as a source of bias.

A secondary source of potential GPCP bias is the relative ice per rain amount, or ice-rain ratio (IRR). GPCP uses the SSMIS 19 and 22-GHz microwave bands to detect precipitation emission over cold ocean backgrounds. While largely transparent to ice, the 19 and 22-GHz ocean measurements have the potential to be affected by ice-scattering in the upper levels, especially in warmer-SST regions that promote deeper convection and more atmospheric ice like the Indo-Pacific warm pool. More ice than average can suppress the emission signal that GPCP relies upon to estimate liquid water content and rainfall, while less ice than average is likely to enhance the estimated GPCP rain. Conceptually, the ice-rain ratio (IRR) is a large-scale measure of ice amount per rain amount. Net monthly ice water path (IWP) is computed from TRMMPR and divided by net monthly TRMMPR precipitation. The IRR anticorrelates with the water balance residual trends, suggesting that larger amounts of ice for a given measure of rain may be partially responsible for GPCP's precipitation underestimation. IRR is a secondary bias actor because it is largely a function of convective organization. The reason it is still necessary as a bias actor is because in the STEI, CRS is relatively flat and does not explain GPCP bias while IRR trends vary much more than in other problem basins and do explain GPCP bias.

There are also times where the water balance residual trend may not be forced by GPCP bias, but rather by SeaFlux evaporation or ERA5 divQ. This study found two convincing trends in the residual term that cannot be confidently attributed to GPCP and are discussed separately in the analysis. These periods are not the norm, however, and are limited to relatively short time scales in specific basins. CRS and IRR are the physical GPCP bias actors, and most water balance residual trends simply respond to changes in these values.

With trends that appear on yearly to decadal time scales, there must be a dynamical driver for these shifts in precipitation states and relative ice concentrations. Here lies the next question: in the fundamental physical parameters of these ocean basin environments, what is forcing the convective states and ice concentrations to change? Each basin has unique characteristics that gives this question non-universal answers. While there are a variety of factors connected to the behaviors of shifting convective states and ice, this work aims to simply connect observations to dynamics, and does not argue that the proposed dynamical explanations are the sole reason for observed shifts. We use three general dynamic factors to explain changes: SST, gradient of SST, and vertical low-level wind shear. The simplest basin to explain is the TCP, where the interplay between shallow and deep organized CRS dictates GPCP bias. The physical mechanism is the El Nino Southern Oscillation (ENSO), which directly controls SST and thus the resulting convective organization/precipitation states. The next basin is the STEI, where CRS is found to be an interplay between deep (isolated + organized) vs shallow states. This is an interplay that would not directly impact GPCP bias on its own, as deep isolated and deep organized convective organization oppose each other in terms of our hypothesized bias framework. Rather, there are larger variations in the IRR trend than in other basins, and these go on to bias GPCP. The trends in STEI CRS are less coupled to SST, and the next-order dynamical actor is low-level (LL) wind shear. Trends in water balance residual, CRS and IRR all prove to be functions of LL shear in the Indian Ocean. Lastly there is the TWP, which sees the Earth’s warmest ocean temperatures. Here, CRS trends are an interplay between deep isolated and deep organized states, directly controlling GPCP bias. The physical drivers behind this convective interplay are complex, as it is not a simple function of the SST and LL shear. This study finds two separate mechanisms that seem related to a fundamental change of TWP SST state. The regular mechanism simply seems to be that LL wind shear controls convective changes in the TWP. When the state changes, however, increased convergence and atmospheric instability seem to maintain steady states of convective organization. Lack of water closure during this period is difficult to explain from a precipitation perspective and may instead be due to either water vapor convergence or evaporation estimates. These dynamical connections are the main findings of this study and will be more deeply explained in the Results section.

CHAPTER 2: DATA AND BACKGROUND

This section provides a summary of all the data used for this study. For our analysis, we rely on three independent water budget component datasets: GPCP for precipitation, ERA5 vertically integrated moisture divergence flux for divQ, and SeaFlux latent heat flux for evaporation. These datasets are not all based on pure observations and remote sensing. GPCP ocean precipitation measurements are based on blended satellite observations, ERA5 divQ is a reanalysis product and SeaFlux uses a neural network to blend satellite-based surface latent heat flux observations with bulk atmospheric dynamics. Detailed descriptions of these datasets can be found in the following sub-sections.

These water budget components come to define our non-closure problem, and we use a convective classification clustering algorithm on TRMMPR and GPM data to create metrics that diagnose the root of this problem. These metrics are CRS and IRR, representing the physical mechanisms that likely bias GPCP. CRS is the classification of ocean scenes into rain states, and we combine it with the rain rate in each scene to determine how much each CRS contributes to the total rainfall in a given spatiotemporal domain. IRR is the ratio between the accumulated PR-measured ice water path and rain rate over all scenes in the same domain. In addition to these metrics, ancillary data is used to deepen bias analyses. The following sub-sections will detail all data used in this study.

2.1: GPCP Precipitation

There are many different data products that hold information about rain rate on a global scale. The main topic of this thesis revolves around climatological changes across a timespan of about 20 years. Previous work has deduced that the Global Precipitation Climatology Project (GPCP) is best suited for the task of non-closure analysis (Koeritzer 2021). This is because GPCP blends precipitation data from multiple inputs while sticking to an overarching goal of serving as a climate data record. Across the record, there are multiple switches between satellite sensors, and the goal entails maintaining temporal consistency with these switches in mind. The result is a continuous high-resolution globally gridded precipitation dataset.

There have been many different versions of GPCP since its 1997 conception, and this study utilizes GPCP Version 2.3 (Adler et al. 2018), which combines three main components: roughly 7000 rain-gauges with satellite microwave and infrared (IR) observations. Since our ocean areas of study have no rain-gauge data, we know that our precipitation observations come mainly from the remaining two sources.

Microwave observations specifically come from the Special Sensor Microwave/Imager (SSMI) that was launched in 1987, and its successors, which include the Special Sensor Microwave Imager Sounder (SSMIS) launched in 2003. GPCP utilizes the 19 and 22-GHz bands on SSMI and SSMIS to make precipitation retrievals using a two-dimensional histogram method. There is an attempt to correct for the beam-filling effect by multiplying rain rate estimates with a coefficient that is a function of the freezing level (Wilheit et al. 1991). SSMI estimates are considered to have lower bias than IR, but it is a polar-orbiting satellite which has low revisit times, leaving temporal gaps that require supplemental information in order to make a quality gridded dataset. Here, geostationary observations are useful in that they provide continuous observations in time. The drawback of these observations is that they are limited to IR bands that are less directly related to precipitation. GPCP thus uses IR only to fill the gaps between microwave passes and any long-term biases are likely to come from the microwave portion of the solution rather than the infrared part. In the few regions that are not covered by geostationary observations, NOAA polar orbiting IR sounders help fill in the gaps (Huffman et al. 1997). In these cases, the IR can be more responsible for any biases. GPCP uses data from various global geostationary satellite operators like the Geostationary Operational Environmental Satellite (GOES), the Geosynchronous Meteorological Satellite (GMS) and the Meteorological Satellite (MeteoSat). GPCP's biggest technological advancement comes in using the higher-accuracy microwave retrievals to bias correct the more frequently sampled IR retrievals. Details about this correction scheme can be found in Adler et al. (1991). The upside of having ocean precipitation measurements mainly from microwave and IR observations is that it makes sources of GPCP bias easier to track and deduce with confidence, as will be seen in the results of this study.

This study also uses the GPCP 3.2 Monthly dataset (Huffman et al. 2022a) published in April 2022, which sees a roughly 6% climatological increase in rain over the tropical oceans compared to V2.3. These increases likely come from increased values of rain over storm tracks. Version 3.2 differs from 2.3 in that it incorporates additional ocean observation calibrations from more modern sensors and algorithms like CloudSat and the Goddard Profiling algorithm (GPROF; Huffman et al. 2022b). As it pertains to water budget closure, Version 3.2 of GPCP shows a climatological improvement over GPCP 2.3. More detailed time series analyses, however, show that bias trends in 2.3 are identical to trends in 3.2, indicating that Version 3.2 did not address the CRS and IRR biases in particular. An analysis of GPCP Version 2.3 vs 3.2 as it pertains to water budget closure is available in the results section.

Koeritzer also considered using the Integrated Multi-Satellite Retrievals for GPM (IMERG) for non-closure analysis. The underlying philosophy differs from GPCP in that

IMERG aims to blend as many precipitation observations as possible for a high resolution best guess of rain rate for a given time. This inherently sacrifices temporal consistency, as this goal is much more sensitive to biases from a wider variety of observational inputs and sensors that change over time. Thus, more sources of bias make IMERG a less favorable choice for non-closure analysis than GPCP V2.3.

2.2: ERA5 Water Vapor Flux Divergence and other ERA5 variables

A reanalysis combines observations with numerical modeling in order to create a temporally consistent, high resolution, globally gridded continuous data product. The European Center for Mid-range Weather Forecast's (ECMWF) Reanalysis 5 (ERA5) is one of a few such products, providing a wealth of self-consistent atmospheric data variables. While the high-resolution nature of reanalysis products is appealing, they cannot be considered fully physical truth. Reanalysis products must continuously balance the state of their model with external observations, and this balance can lead to different outputs that can vary over time. ERA5 itself outputs precipitation, evaporation and water vapor divergence. A closure analysis that uses just ERA5 components shows much flatter trends in the residual term, indicating that the ERA5 model has internal closure, but it is neither perfect, nor required as observations continuously modify the model states. Several authors have also pointed out that ERA5 precipitation appears to have too much light precipitation in the tropics (Stephens et al. 2010) while also creating too much evaporation when compared to in-situ observations (Robertson et al. 2020). For this reason, this study focuses on ERA5 water vapor divergence. To the extent that both water vapor and winds are central to the global weather, it is likely that divQ is unbiased even when ERA5 produces slightly more P and E than satellite observations of the same parameters.

Prior work considered the use of other reanalysis products like the Modern-Era Retrospective analysis for Research and Applications Version 2 (MERRA-2) but discovered the presence of a data artifact in 2010 (Koeritzer 2021). Since no data artifact was found in ERA5, and water vapor trends closely matched observations, it serves as a better candidate for a temporally consistent closure analysis.

2.3: SeaFlux Evaporation

This study uses the SeaFlux dataset (Clayson et al. 2015) for closure analysis. An additional reason that this study is only conducted over oceans is because land closure analyses would have to use evapotranspiration instead of evaporation, making the problem more difficult to analyze. Getting observationally based globally gridded values of evaporation differs from precipitation in that there is no single satellite measurement that can be made that translates cleanly into an evaporation value. Instead, evaporation is converted from latent heat flux, which is calculated from the bulk aerodynamic formula described below.

$$LH = \rho L_v c_e U(q_0 - q_a) \tag{3}$$

This formula was derived for the Coupled Ocean-Atmosphere Response Experiment (COARE) (Fairall et al. 2003). LH is the latent heat flux, ρ is the air density, L_v is the latent heat of water vaporization, c_e is the turbulent transfer coefficient, U is horizontal surface wind speed, and q_0 and q_a are specific humidity at the surface and at a reference height, respectively. The reference height is usually at 2 or 10 meters above the surface. SeaFlux does the work of bringing together observations from different remote sensing data to get a globally gridded high resolution latent heat flux product over ice-free oceans, as well as the bulk dynamic variables. q_0 over the ocean is just the saturation specific humidity for the SST and L_v has a small SST dependence. These two values are thus only functions of SST, which SeaFlux obtains from the OISST Version 2. This dataset is also referred to as the Reynolds' SST, and it retrieves SSTs using the Advanced Very High Resolution Radiometer (AVHRR) infrared satellite (Reynolds et al. 2007). This dataset is treated as the base SST product but is then linearly interpolated to create a 1-hourly SST product that captures the diurnal cycle. U is input from an adjusted version of the NASA Cross-Calibrated Multiplatform (CCMP) winds (Clayson and Bogdanoff 2013).

SeaFlux is unique from other products in its approach to q_a. q_a is not a simple function of SST, and the best way to get it is through its relationship with precipitable water. Multiple linear regression has shown to functionally retrieve q_a through precipitable water (Liu 1986), but this method fails to capture the nonlinear relationship between the two values. Thus, SeaFlux uses machine learning trained on buoy networks to output q_a. Details on this neural net can be found in Roberts et al. (2010), and more information on the details of SeaFlux overall can be found in Clayson et al. (2015). There are weaknesses to this machine learning method. While the algorithm shows a drastically lower root mean squared error (RMSE) than other methods, accuracy is reduced for high wind speed and very cloudy situations. Solving this is difficult because the relationship between precipitable water and near-surface humidity q_a is still not well understood, and so the problem becomes ill posed. Regardless, Koeritzer found SeaFlux's lack of reliance on models to be preferable from a bias analysis standpoint, showing that it is the best candidate for this closure analysis study (Koeritzer 2021).

2.4: Convective States, IRR, and merging TRMM-GPM

The K-means clustering algorithm used in Elsaesser et al. (2010) works with five parameters retrieved from TRMMPR to classify scenes of convection into convective rain states (CRS). Each vector that goes into the five-dimensional clustering space represents convective characteristics from 1x1° tropical ocean boxes seen by TRMM. One of the parameters is the number of convective pixels with echo top heights below 5 kilometers divided by the total number of pixels in the ocean box. The next two parameters are the same except for echo tops between 5 and 9 km, and then greater than 9 km. The fourth parameter is the average rain rate of all convective pixels in the box, otherwise known as convective rain rate. The fifth and final parameter is the ratio of convective rain rate to the rain rate of all pixels in the box. Elsaesser found that the choice of 3 CRS – defined as shallow, deep isolated, and deep organized – capture most of the convective rainfall while remaining self-similar over the Earth's tropical ocean basins. Henderson et al. (2017a and 2017b) was able to expand upon this robust classification system, adding a 4th classification that specifically identifies scenes of exclusively stratiform rainfall, and used this to evaluate the sensitivity of various TRMM rainfall products as a function of convective type. This work focuses on biases that stem from convective organization and doesn't make use of the 4th stratiform classification utilized in Henderson's work as it was rare and simply a result of stratiform precipitation that remained from nearby convection. We use the CRS to create a rainfall metric for closure analysis: the fraction of precipitation that each CRS contributes to total rainfall each month.

Elsaesser's convective clustering algorithm was designed for TRMM data. Henderson's bias analyses involved adapting Elsaesser's clustering algorithm to the Kwajalein KPOL GV ground radar (Henderson et al. 2017a), displaying the flexibility of the clustering concept. The

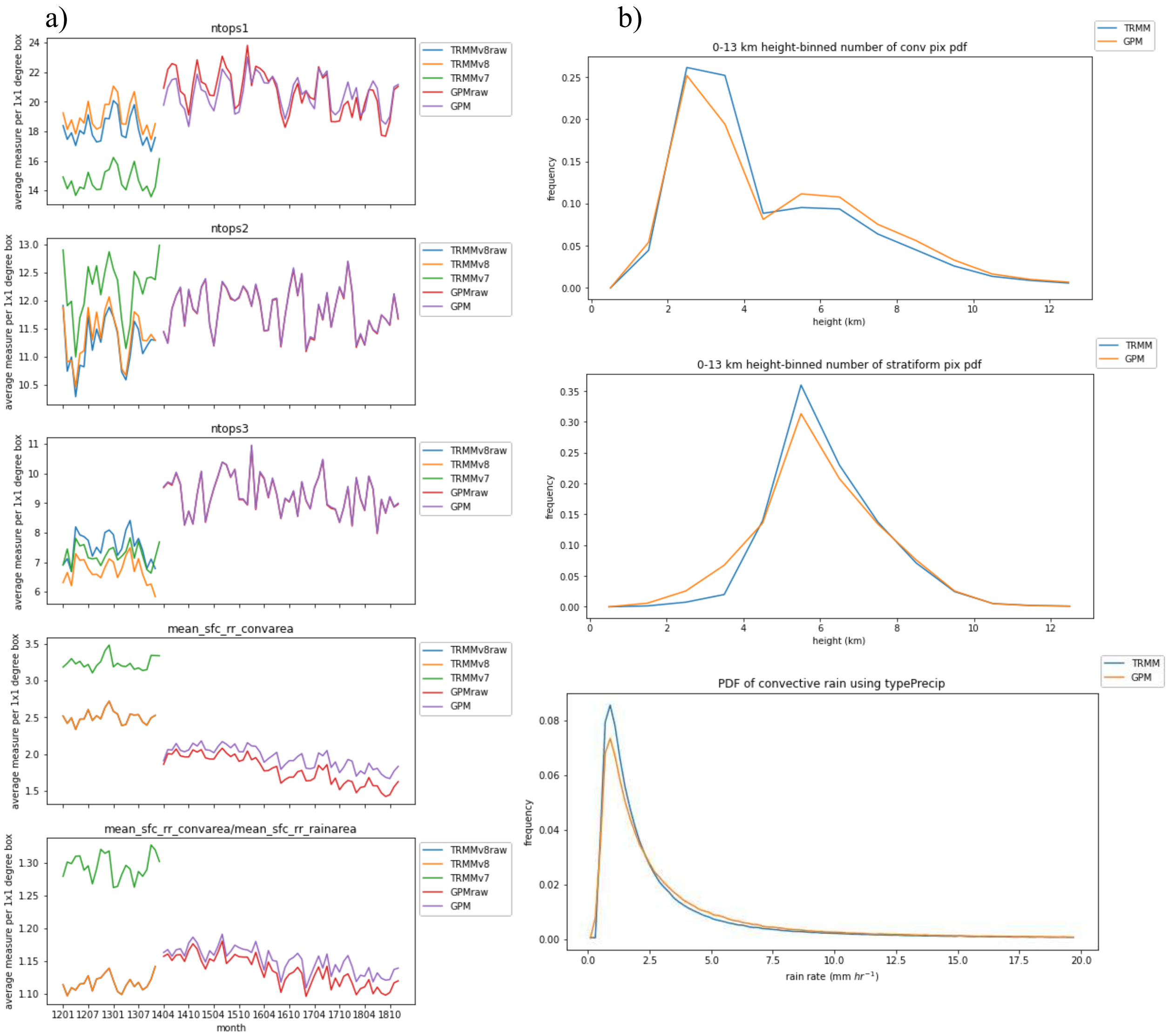

Figure 4: Discrepancies in the five clustering parameters between TRMM and GPM are shown in a), where the 'raw' suffix indicates using raw reflectivity measurements rather than attenuation corrected. A more implicit difference between TRMM and GPM is visible in b) where GPM (TRMM) classifies more pixels as convective (stratiform), and TRMM sees more convective pixels with smaller rain rates.

GPM satellite was built as a successor to TRMM, and the KuPR instrument onboard GPM measures all the same things as TRMMPR, meaning the same clustering algorithm should be applicable to GPM data. However, when time series of these parameters from TRMM and GPM are compared (Fig. 4a), there is a discrepancy between the end of the TRMM and beginning of the GPM satellite time series, as well as the averages of each time series in these clustering parameters. These inconsistencies would have cascading effects when it comes to getting a consistent CRS time series across the two satellites eras.

Initially, several changes to the TRMMPR clustering algorithm were made to try to address parameter discrepancies. TRMM samples swaths every 0.6 microseconds while GPM samples every 0.7 microseconds. This affects the total number of pixels in a 1x1° box between TRMM and GPM and must be accounted for. The original Elsaesser TRMMPR clustering algorithm uses a 17 dBZ reflectivity threshold to define precipitation top heights. Attenuation-corrected measurements of reflectivity were used in the original algorithm, but a change was made to use the raw measurements of reflectivity as they match much better between TRMM and GPM. One caveat in using the raw reflectivity is that, at a certain height, the radar beam interacts with the Earth's surface, causing clutter in the trend and rendering the reflectivity measurement useless. A change is made to the clustering algorithm so that any raw measurement below this clutter height is not considered. Unfortunately, a few key instrument differences between the TRMM and GPM satellites require additional changes in the algorithm to bring consistency between the two precipitation measurement missions.

A study by Seto et al. (2022) finds that KuPR overall detects 1.3% more net precipitation than PR. This is because KuPR's minimum reflectivity threshold was unexpectedly determined to be 15.46 dBZ whereas PR's is 20.21 dBZ. Additionally, KuPR operates at 13.8 GHz while PR operates at 13.6 GHz. The difference in operational frequency is found to affect heavy precipitation estimates and the difference in sensitivity affects precipitation totals and frequency. It is likely that these differences are also responsible for the convective/stratiform pixel partitioning discrepancy between TRMM and GPM (Fig 4b). These discrepancies between the two satellites are on the instrument level rather than the retrieval level, they are not easily addressable by small changes in the clustering algorithm. In order to get convective classification consistency across the two missions, a constant offset was applied to GPM clustering parameters to ensure consistency across the time series between the two satellite missions. This offset was determined using the difference in average values over the four months of overlap between TRMM and GPM, April-July 2014. This forces the GPM CRS averages during the overlap to match TRMM and extends to the rest of the GPM time series. Given that CRS are used merely to explain the overall nature of the observed biases, we benefit from the explicit removal of possible instrument biases.

Next is the IRR, which utilizes variables from the same TRMMPR and GPM KuPR Level 2A products as the K-means clustering algorithm. IWP is summed over all scenes and divided by the sum of surface rain rates over all scenes in a month to return a qualitative proxy for monthly ‘ice per raindrop,’ which will be useful in considering potential microwave ice-scattering bias. Table 1a illustrates the mean IRR value associated with each CRS across the six ocean basins. There is a surprising result from this breakdown of IRR: the ratio that is attributable to shallow rain state is comparable to the ratios of the deep states, and greater than both deep states in the STEI and TWP warm pool basins. These results contradicted our notional understanding of the shallow state and warranted further explanation. Figure 5 shows contoured frequency by altitude (CFAD) diagrams of precipitable water content over the STEI. Average profiles were calculated for each ocean scene using the TRMMPR and GPM KuPR Level 2A profiles of precipitation rate. The non-zero values of these profiles were then input into a 2-dimensional histogram of height and rain rate and contoured to get the CFADs. This plot reveals that the frequency of occurrence of precipitation above the freezing level in the shallow state is enough to rival the deep states, while remaining rare from an average statistical standpoint.

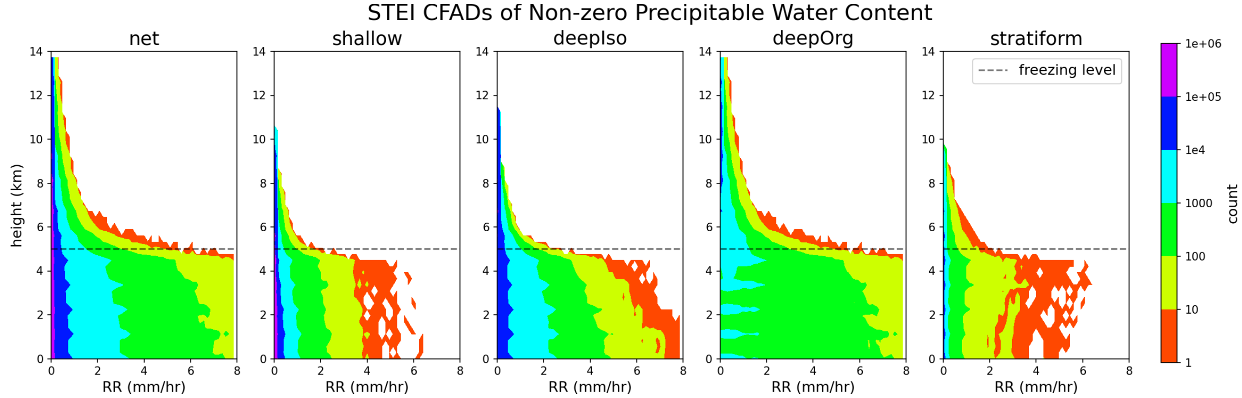

Figure 5: Contoured frequency by altitude diagrams (CFAD) of precipitable water content for each CRS in the STEI using a logarithmic color scale. An approximate freezing level of 5 km is included to indicate likely concentrations of ice vs liquid precipitation.

Table 1: a) Monthly mean values of accumulated IWP and rain rate, and the resulting IRR for each CRS in each ocean basin. Units of net IWP values are in kg/m^2 while values of net rain rate are in m/hr. b) Standard deviation of the smoothed IRR time series in each basin for each CRS

Monthly Mean $\frac{\sum IWP}{\sum RR} = IRR$

CRS	TWI	STEI	TWP	TCP	TEP	TAO
shallow	$\frac{18.3}{73.9} = 0.25$	$\frac{19.5}{63.8} = 0.31$	$\frac{44.9}{134} = 0.34$	$\frac{25.2}{126} = 0.20$	$\frac{19.9}{69.1} = 0.29$	$\frac{19.1}{75.5} = 0.25$
DeepIso	$\frac{36.0}{116} = 0.31$	$\frac{40.2}{133} = 0.30$	$\frac{110}{339} = 0.33$	$\frac{32.7}{133} = 0.25$	$\frac{35.4}{117} = 0.30$	$\frac{37.3}{146} = 0.26$
DeepOrg	$\frac{18.8}{79.5} = 0.24$	$\frac{21.5}{96.3} = 0.22$	$\frac{60.7}{273} = 0.22$	$\frac{17.2}{83.7} = 0.21$	$\frac{23.4}{98.0} = 0.24$	$\frac{19.3}{84.9} = 0.23$
strat	$\frac{4.11}{1.87} = 2.2$	$\frac{5.72}{1.80} = 3.2$	$\frac{11.6}{5.7} = 2.0$	$\frac{7.62}{1.38} = 5.5$	$\frac{5.45}{1.72} = 3.2$	$\frac{7.82}{1.94} = 4.03$
Net	$\frac{77.3}{271} = 0.28$	$\frac{87.0}{295} = 0.29$	$\frac{228}{752} = 0.31$	$\frac{82.7}{344} = 0.24$	$\frac{84.0}{286} = 0.28$	$\frac{83.5}{308} = 0.28$

12-month Smoothed IRR Standard Deviation

CRS	TWI	STEI	TWP	TCP	TEP	TAO
shallow	.023	.025	.020	.013	.017	.023
DeepIso	.019	.020	.011	.021	.014	.011
DeepOrg	.016	.010	.010	.022	.034	.011
strat	2.6	6.5	.49	6.6	29	2.6
Net	.020	.020	.010	.016	.015	.011

2.5: Ancillary Data

Each ocean basin has a different dynamical environment that controls convective organization and the amount of ice. To determine these fundamental drivers, this study heavily relies on ERA5 reanalysis data for dynamic variables like wind speed, convective available potential energy (CAPE), convective inhibition (CIN) and boundary layer height (BLH). The Optimum Interpolation Sea Surface Temperature (OISST; Reynolds et al. 2007) is used to calculate SST gradient. To quantify the effect of El Nino, the Nino3.4 index is used (Trenberth and Stepaniak 2001). There are several other data sources that were used to interpret water balance residual trends that came from SeaFlux evaporation and ERA5 divQ rather than GPCP bias. Specifically, the Smith and Reynolds ERSST (NOAA 2018), ERA5 and SeaFlux SSTs were all compared to determine that the SeaFlux evaporation is largely responsible for the trend from 2016 to 2020 in the STEI basin. Additionally, the Modern-Era Retrospective Analysis Version 2 (MERRA-2; GMAO 2015), Quick Scatterometer (QuikSCAT; SeaPAC 2020), SeaFlux and ERA5 surface winds were all compared to argue that ERA5 divQ is possibly responsible for the trend from 2001 to 2007 in the TWP basin.

CHAPTER 3: DISCUSSION OF RESULTS

There are two key conceptual properties of water balance residual that are helpful in this closure analysis. The first is the mean of the water balance residual time series in any given basin, which is referred to as the magnitude of residual. Interesting questions arise when comparing magnitudes of the residual in different basins, as in Figure 8 where magnitudes are plotted as a function of longitude. For example, why is magnitude of the residual term positive in the Indian Ocean basin and negative in the Pacific? The second property is how long and to what extent the water balance residual curve deviates from the mean in each basins' time series, and this will be referred to as the trends in water balance residual. For example, why does the West Pacific residual time series have a positive trend between 2011 and 2016 (Figure 2)? Usage of these 'magnitude' and 'trend' terms will also be extended to other values like CRS, IRR, SST, shear etc.

This study will largely focus on trends in residual, with less attention on magnitude. This is because magnitude of the residual is more easily mutable. Appendix Figure S1 shows residual trends using GPCP V2.3 and using V3.2. The biggest improvement in closure with V3.2 is over the TWP, where the magnitude of the residual is much closer to 0. However, overall closure was worse over the STEI and TAO basins where the magnitude of V3.2 is further from zero. There are very few changes in the remaining basins in comparing water balance residual using V2.3 vs V3.2. In fact, the only differences in residual output between the products is in relative magnitude, while the temporal trend is nearly identical in the two versions. GPCP V3.2 had many justifiable reasons to make the changes it did (Huffman et al. 2022b), but these changes did not address long-term trends in non-closure.

Following Brown & Kummerow (2014), the STEI and TWI ocean basins were originally a single box centered in the middle of the Indian Ocean. This single box was considered to summarize the extent of closure lack in the whole tropical Indian Ocean and had very small water balance residuals in the Brown & Kummerow study. However, a single box in the middle of the Indian Ocean fails to account for effects of the Indian Ocean Dipole (IOD). The IOD is a pattern of variability that sees anomalously low/high temperatures in the East Indian Ocean pair with anomalously high/low temperatures in the West Indian to impact wind and rain patterns. This variability is independent from ENSO and unique to the Indian Ocean (Saji et al. 1999). One key improvement that this study makes upon Brown and Kummerow is using this dynamic climatology to inform closure analysis box locations. The prior central box location contained elements of both sides of the dipole, resulting in a muted residual line that showed very little trend. By replacing the old box with two boxes that instead capture the two sides of the IOD (Fig. 6; Fig 1), we see the STEI become a 'problem basin' in terms of residual trend (Fig 2).

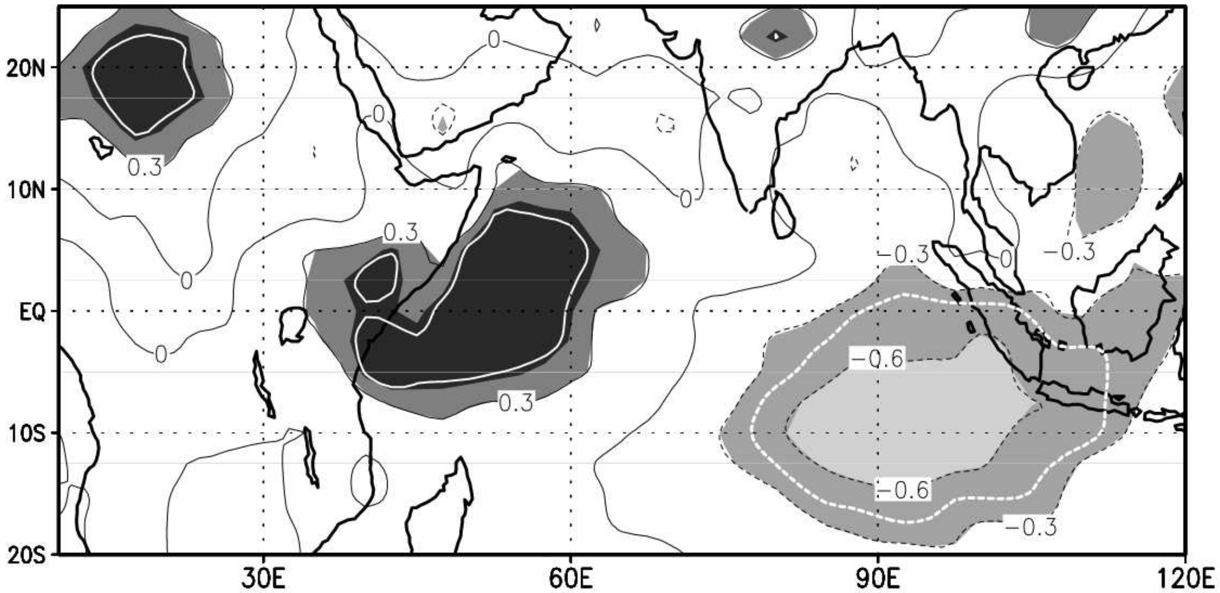

Figure 6: Correlation of the Dipole Mode Index (DMI) with rainfall, courtesy of Saji et al. (1999). The non-closure trends in the tropical boxes in the Indian Ocean become more explainable when constrained to the east and west areas of activity.

3.1: Analysis Across All Basins

Water balance residual is a combination of three terms: GPCP precipitation, ERA5 divQ and SeaFlux evaporation. The first step in this analysis is to examine each term's relationship with non-closure trends. Because there is a linear relationship between the individual terms and water balance residual, checking the Pearson correlation of each term with the residual helps identify avenues for exploration. Table 2 reveals that GPCP rain has the highest correlation values with water balance residual across all basins. Even though these correlations are normalized comparisons, it could be the case that GPCP precipitation simply has the highest amplitude variations that unfairly weight the residual line, masking potential trends from the other water budget components. However, by looking at the residual plotted against the three components (Fig. 7), divQ in the TWP has variations of similar amplitude but maintains a much smaller correlation with water balance residual; this divQ behavior is similar across all basins. While there are marked examples that will be discussed of divQ and evaporation having errors that influence closure, the consistently positive higher correlations suggest that precipitation error is a worthy avenue to explore as a source of non-closure. Evaporation is relatively flat, and likely doesn't contribute much to large trends in water balance residual in the face of larger GPCP and divQ variance.

Table 2: Correlations in each basin of water balance residual with the three budget components. GPCP's correlations are the largest in magnitude and most consistent in sign.

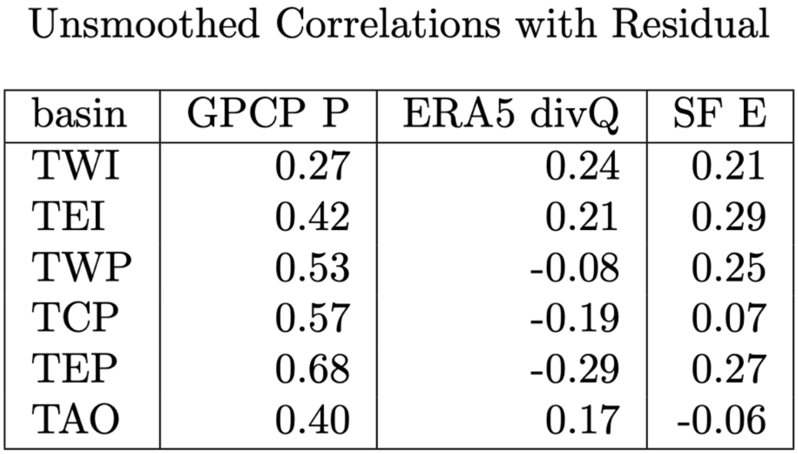

Unsmoothed Correlations with Residual

basin	GPCP P	ERA5 divQ	SF E
TWI	0.27	0.24	0.21
TEI	0.42	0.21	0.29
TWP	0.53	-0.08	0.25
TCP	0.57	-0.19	0.07
TEP	0.68	-0.29	0.27
TAO	0.40	0.17	-0.06

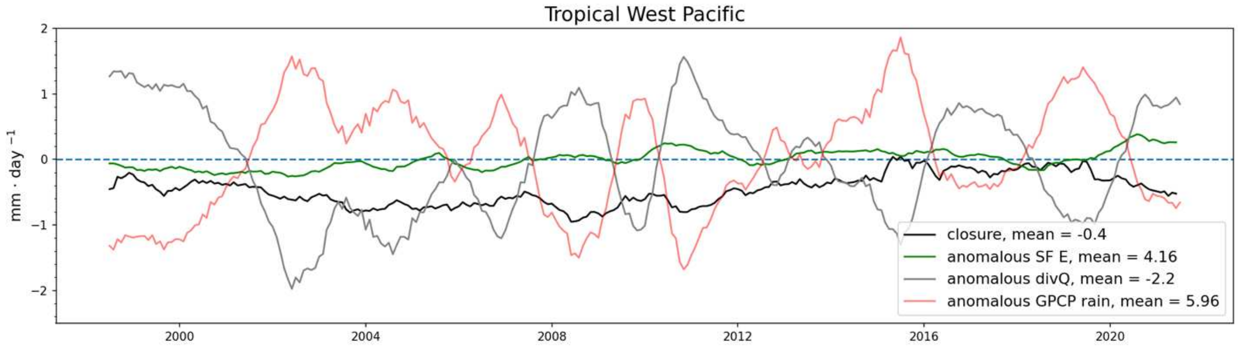

Figure 7: Water balance residual plotted alongside water budget components in the TWP.

Convective rain state is the main mechanism hypothesized in this study to bias GPCP rain estimates. There are three CRS: shallow, deep isolated and deep organized. These three convective regimes come from the Elsaesser et al. (2010) convective classification scheme. Henderson et al. (2017a and 2017b) found rain rates to be systematically biased as a function of convective regime, concluding that deep isolated convective rain is generally underestimated, and deep organized stratiform rain is overestimated by TMI over locations in the tropical western Pacific and central Indian oceans. While Henderson et al. (2017b) compared to a different passive microwave algorithm than GPCP, he attributed the biases to fundamental properties of microwave instruments that are likely also present in the GPCP product. The bias effect from each CRS is examined through its percentage of rain contribution for each month. The precipitation term in the closure framework equation is positive (Eq. 2), so deep organized rain contribution should correlate with the residual trend because it is overestimated, while shallow and deep isolated rain contribution should anti-correlate with the residual because they are underestimated.

The following sections of this results discussion will use CRS to explain non-closure in the TCP, TWP and STEI problem basins. Water balance residual and CRS trends in these problem basins are numerous and high amplitude. In contrast, residual trends in the non-problem basins (TEP, TAO, and TWI) are lower in amplitude and fewer in frequency (Fig. 2). While these non-problem basins each contain examples of non-closure likely forced by CRS, they overall lack trends in the longer-term residuals, and thus are less of a consideration in this study.

CRS may be the main driver of non-closure, but the different thermodynamic environments of each problem basin must be explored in order to understand why CRS is changing in the first place. For this dynamical investigation, SST will be the primary value of interest. SST is a fundamental dynamic driver of convection (Zhang 1993), but it impacts each basin differently, warranting a second variable for clearer analysis: low-level (LL) wind shear, a key component in thunderstorm formation and convective processes (Houze 1994). For this study, low-level wind shear is defined as the magnitude of the wind vector difference between the 700 and 925 hPa pressure levels from ERA5. With this basin and dynamical analysis framework in mind, let us begin dissecting the problem basins.

3.2: The Tropical Central Pacific

The Tropical Central Pacific water balance residual trends largely stem from an interplay between shallow and deep organized CRS. Relative to rest of the tropical oceans, the TCP has the highest average presence of shallow rain state (Fig. 8), with the dominant mode in the time series switching between shallow and deep isolated, and with deep organized staying relatively low but more variable than deep isolated (Fig. 9). Shallow CRS in this basin has the highest overall variability among the three rain states, exhibiting a strong negative correlation with the residual trend. During El Nino events in 2010 and 2016, the shallow CRS decreases with corresponding increases in deep organized and deep isolated states, and a corresponding improvement in the residual trend. During the La Nina periods of 1999, 2007-08, and 2011-12, we see shallow CRS dominating with a corresponding low residual trend. Out of the three problem basins, the TCP is the simplest to explain, because all trends and patterns follow ENSO.

If we assume that the SeaFlux evaporation and ERA5 divQ are correct, and GPCP is the only source of error in the trends and magnitude of the TCP water balance residual, then a bias correction can be implemented by just using the convective rain states. More specifically, a 20% decrease in deep organized rain contribution combined with a 10% increase in deep isolated, and a 40% increase in the amount of shallow rain contribution act to flatten trends in the residual term, improving the water budget closure over the TCP. This is not a proposed solution to the problem, but rather shows that reasonable bias magnitudes would explain the lack of closure given the biases found by Henderson et al. (2017b).

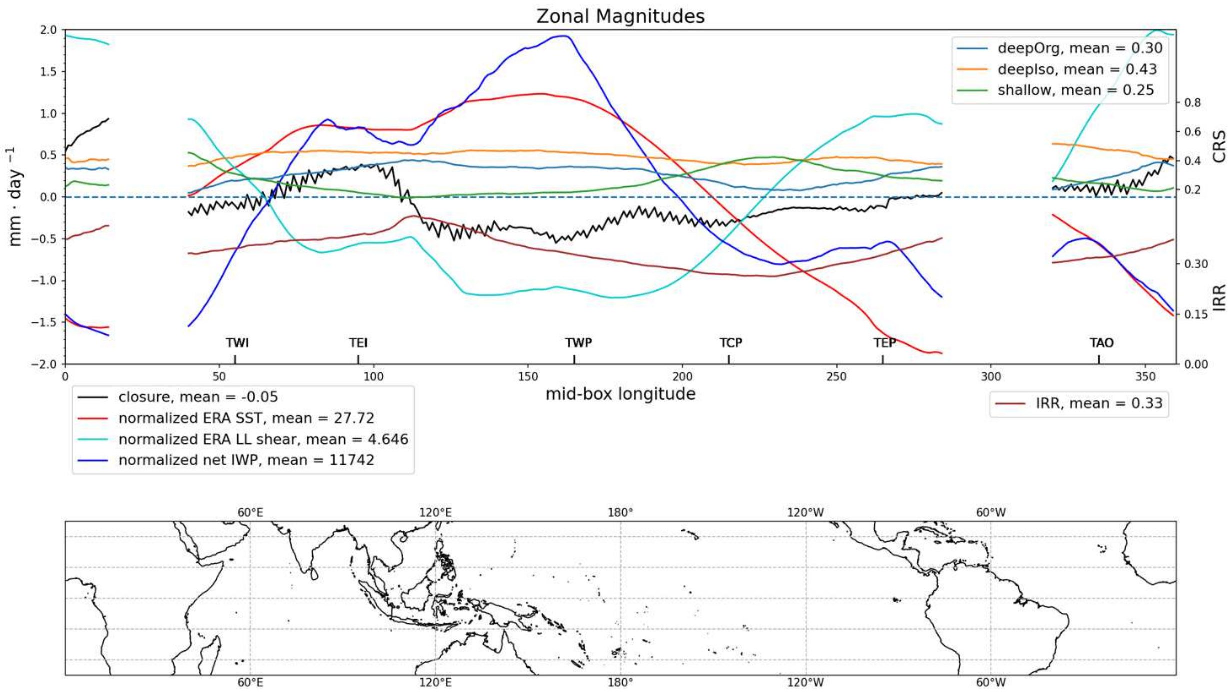

Figure 8: CRS and IRR bias actors, as well as dynamic mechanisms plotted as functions of longitude. Each point represents the mean value of the 20-year time series in a 30x30 degree box centered at the longitude value on the x-axis. A land mask has been applied to all data, and so boxes near/on land masses have very little information content and can be treated as discontinuities.

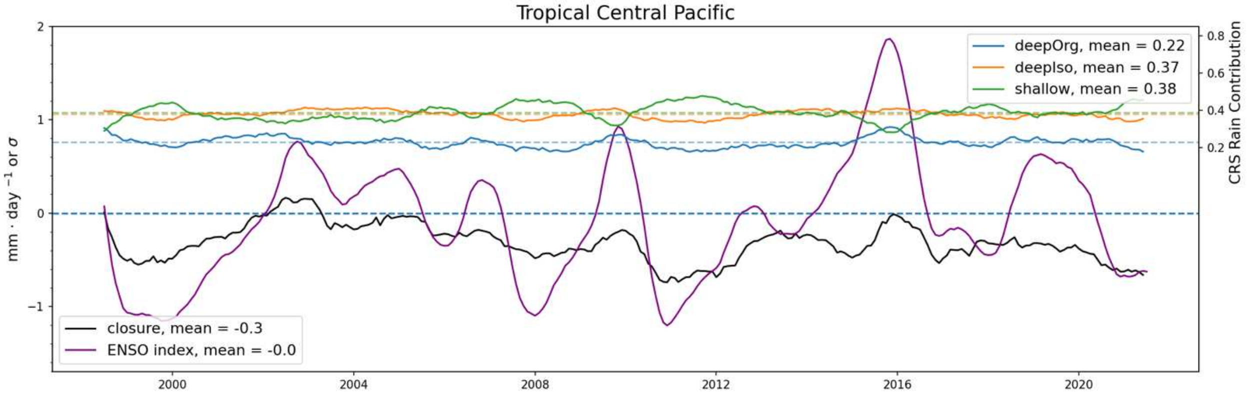

Figure 9: Tropical Central Pacific water balance residual trend is controlled by the interplay of deep organized and shallow rain state, both of which are highly correlated with the Nino3.4 index.

Now we must explore the dynamical reasons behind CRS trends in the TCP basin. Figure 9 shows that the biggest trends in residual and CRS correspond to the ENSO Nino3.4 index; during each El Nino, deep convection increases, and during La Nina, shallow convection dominates. ENSO is an SST-circulation mechanism, where anomalously warm waters during El Nino couple with the Walker circulation and provide the heat source necessary for deeper atmospheric dynamics. Thus, ENSO controls large shifts in convective organization. The warmer

TCP SSTs during El Nino provide heat necessary deeper convection, promoting higher deep organized and deep isolated, and lower shallow CRSs.

3.3: The Tropical West Pacific

The West Pacific water balance residual stems primarily from an interplay between deep isolated and deep organized rain state (Fig. 10). The residual series starts with a negative trend, stays significantly negative from 2000-2011, and then slowly rises with a positive trend from 2011-16, showing good closure in the 2016-2020 timeframe, but again reversing after 2020. The poor closure period is also when the deep isolated CRS dominates precipitation. The first time we see deep organized dominance is in late 2015, when the residual rises during a strong El Nino warming. Then it takes a small dip out of closure as deep isolated dominance returns, and then once again returns to closure as deep organized dominates once again. Beyond 2020, poor closure is again evident as deep isolated convection dominates. Outside of these anomalies in deep organized dominance, deep isolated reigns strongly, especially during La Nina periods. This causes an overall underestimation which keeps the residual negatively biased, most prominently during the La Nina periods surrounding the El Nino in 2010.

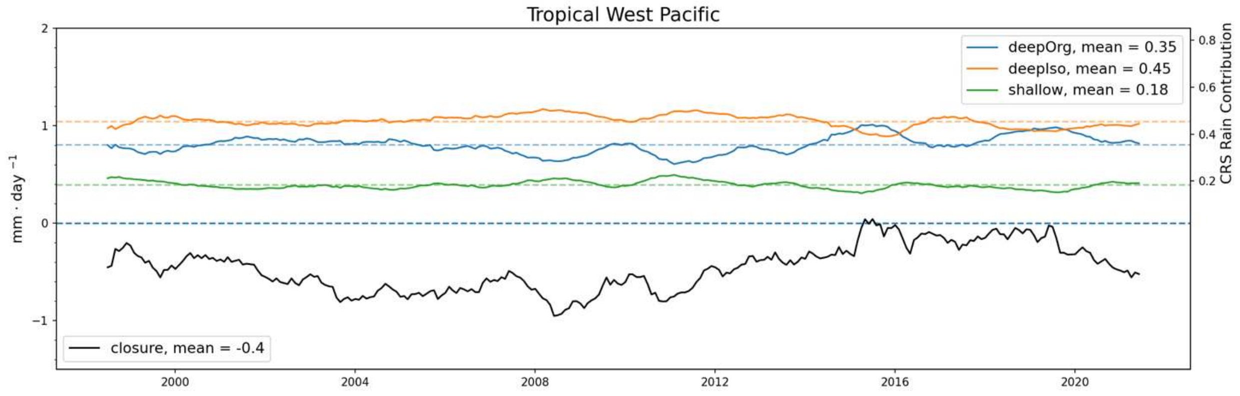

Figure 10: The bias in the TWP is primarily caused by the interplay of deep organized and deep isolated rain states.

CRS rain partitioning does not explain all residual behavior, the 2001-2007 period has an important nuance. The deep organized and deep isolated CRS lines are trendless and close together during this period, yet water balance residual has a negative trend (Fig. 10). Those two CRS lines are similarly close in 2016-2018, but the residual line is more closed and responsive to their trends, adhering to the hypothesized bias framework. The interplay between deep organized and deep isolated CRS is the convective proxy explanation for non-closure GPCP bias in the TWP, and it explains the behavior of the water balance residual trends, save for 2001-2007. There are no significant IRR trends during 2001-2007 to impact the residual, implying that another bias actor may be impacting GPCP, divQ and/or evaporation during the period.

The mean CRS characteristics of the West Pacific basin are completely different from the Central, and yet the GPCP contribution can be explained by the same bias framework. Instead of shallow convective dominance found in the Central Pacific, the warmer TWP SSTs promote deep isolated dominance with occasional relinquishment to deep organized systems. In the spirit of speculative bias correction, a 40% decrease in deep organized rain contribution combined with a 40% increase in deep isolated, and a 15% increase in shallow rain contribution would act to maintain closure in this basin. While these correction values are different from the Central Pacific, this is not an argument for regional bias corrections. It indicates rather, that while the bias direction of each CRS is consistent among basins, biases cannot be addressed by simply assigning global correction factors to each CRS.

The TWP non-closure and bias actors are not simply related to SST, as they were in the Central Pacific, nor LL shear (Fig. 11). Yet, closure and convective dependencies on shear and SST in the TWP are not completely random/uncorrelated either; CRS values show some SST dependence, but the consistent mix of strong low and high values near 29.3° C SST across the

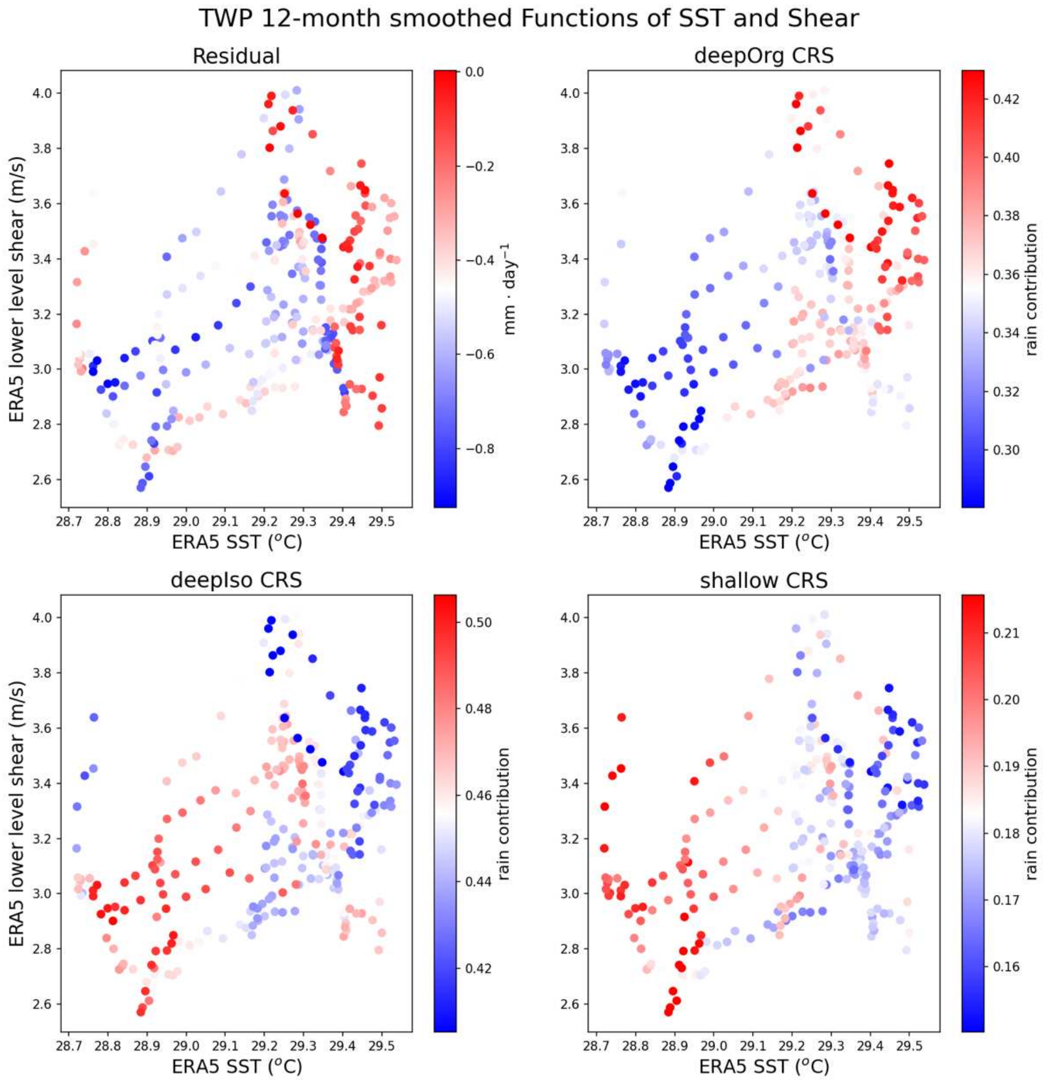

Figure 11: TWP residual and bias actors plotted as functions of SST and shear.

residual and bias actor plots weakens the relationship. Investigating stability terms from ERA5 like convective available potential energy (CAPE), convective inhibition (CIN) and boundary layer height (BLH), as well as SeaFlux evaporation and surface differential humidity (dq) yield similarly mixed results (Fig. S2). These variables come from a variety of independent data products, but they all agree on a bifurcation in roughly the same SST-shear space. This indicates that the dynamical reasoning for changes in TWP convection may be more related to changes in a large-scale state rather than dependencies on just a couple of dynamical variables.

The first step in exploring this perspective more deeply involves artificially extending the beginning of the TWP residual line. Earlier in this Results section it was noted that out of the three components that comprise the water balance residual, evaporation overall does not contribute significantly to its trend as it is relatively flat and constant. The primary reason that the residual time series in this study is limited to beginning in 1998 is because the SeaFlux evaporation product starts in 1998. A secondary reason is that TRMM did not launch until 1998, making the satellite-based CRS and IRR analysis impossible to conduct pre-launch. ERA5 variables and GPCP precipitation, however, both range from 1979-present. Given that SeaFlux evaporation does not significantly contribute to most residual trends in this basin, it becomes possible to artificially 'go back' in the TWP by replacing SeaFlux evaporation with ERA5 evaporation. There are dangers and limitations to this method. The SSMIS series did not launch until 1987, casting reasonable doubt upon GPCP data before then. For our purposes, however, this becomes a useful qualitative tool to further evaluate the TWP.

Figure 12a shows the original residual line with the ERA5 evaporation version overlaid and extending back to 1987. This longer closure record adds new perspectives into the TWP analysis: the basin was well-closed before 1998, and the decadal low trend period starting around the year 2000 looks more like an anomaly rather than the norm. Overlaid onto that is the Nino3.4 index as well as the average TWP SST. One factor that stands out from this perspective is how the poor closure trend is bookended by two very strong El Nino events, with an overall weaker ENSO index taking place during the low. An additional clue appears when considering the TWP average SST in relation to ENSO. The conventional thinking surrounding ENSO is that as the warm tongue extends into the central and east Pacific, west Pacific SSTs see anomalous lows (Solomon and Jin 2005), implying that there should be a general inverse relationship that sees

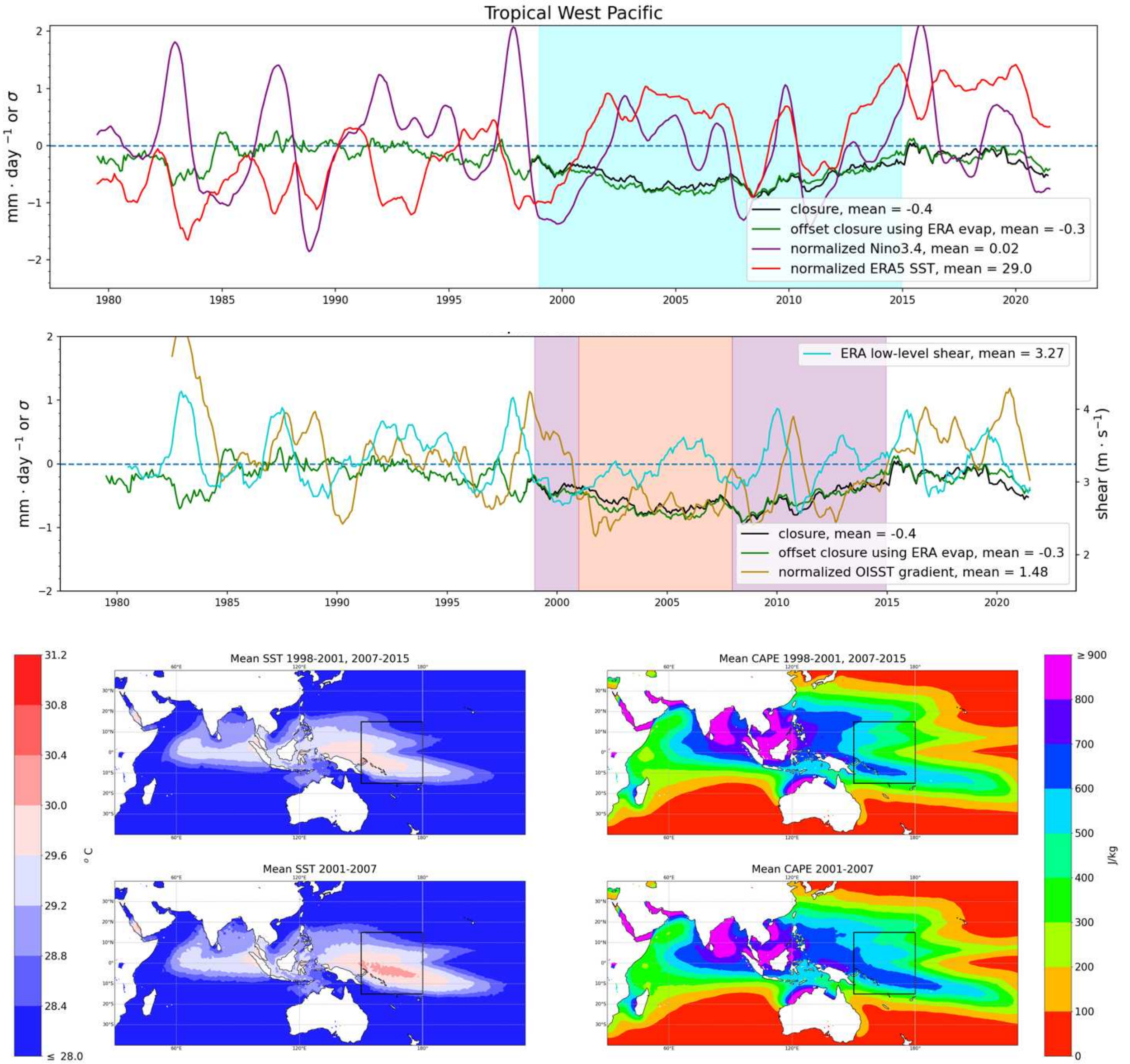

Figure 12: a) TWP SST (anti) correlates with the Nino3.4 index (outside) during the period of low closure. b) The SST gradient and LL shear as well as the dominant periods of the two proposed mechanisms, purple highlight indicating that low-level shear dominates deep organized convection and orange highlight indicating when convergence of water vapor controls deep organized convection. c) The mean SSTs and convective available potential energy (CAPE) during the periods of the two proposed mechanisms.

highs in the Nino3.4 index match with lows in the TWP SST. Outside of the decadal low closure period, this relationship generally seems to be the case, however during the period, TWP SST generally tracks with the Nino3.4 index roughly between the strong El Nino events of 1998 and 2015. There are generally two types of ENSOs that exhibit significantly different behaviors, Central vs East Pacific ENSO (Kao and Yu 2009). The two El Nino events that bookend this period of TWP SST behavior were categorized as EP ENSOs, while all the events that happened in between were considered CP ENSOs (Zhang et al 2019). This unusual SST state behavior in the TWP seems related to ENSO types and coincides roughly with the global warming ‘hiatus’ period observed from 1998-2013 (Allan et al. 2014; Amaya et al. 2015). Potential causal links of this period’s SSTs with convection will now be explored.

We posit that in the TWP, SST gradient is the most fundamental driver of convective changes. It is not as simple as the SST argument used to explain the TCP, as it seems there are two different kinds of SST gradient that lead to two distinct convective-controlling mechanisms

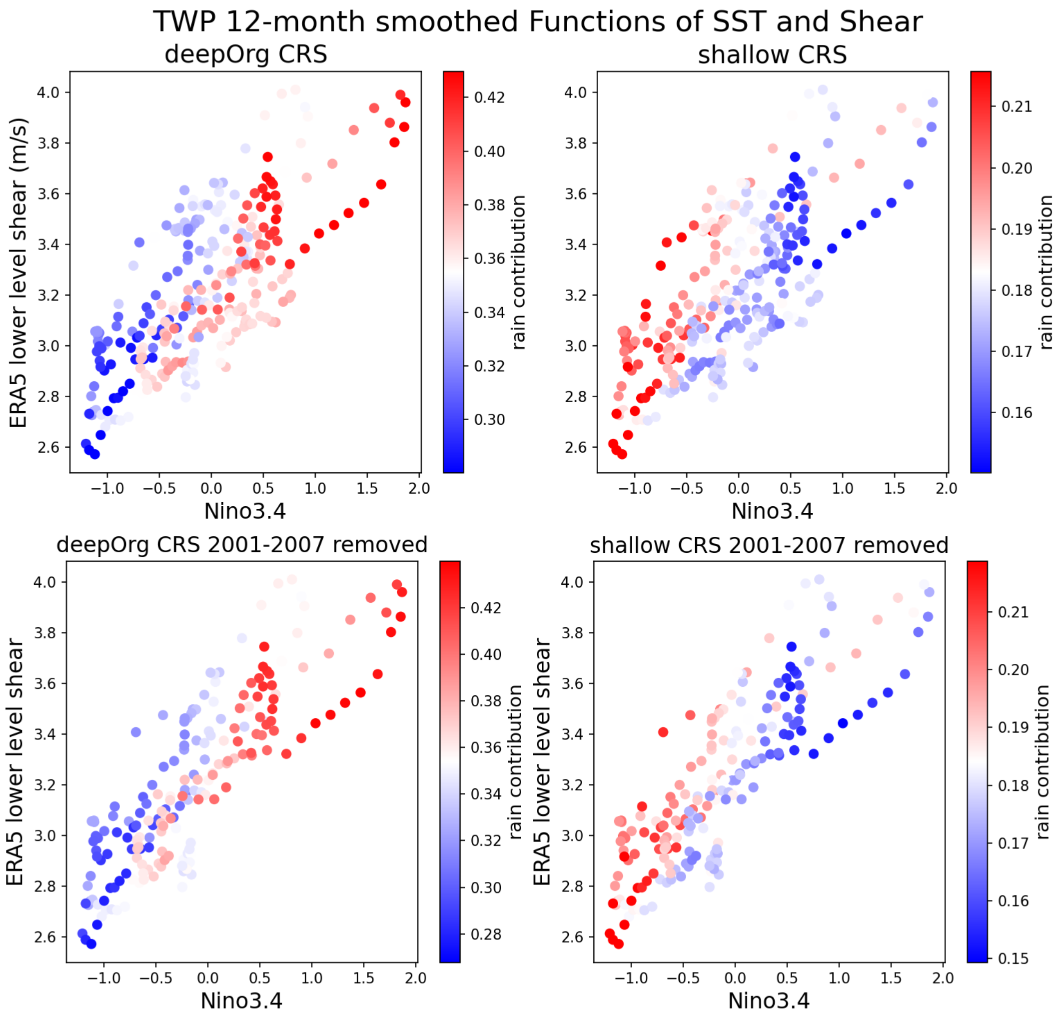

Figure 13: Removing the time period when the convergence mechanism dominates over the LL shear mechanism illuminates the linear relationship between LL shear and ENSO. Additionally, the deep organized CRS is shown to be a better function of LL shear and ENSO outside this time period. Residual and the other CRS’ show similar improvements in dependency when the convergence period is removed.

that dominate at different periods of time. The first mechanism is ENSO and its impact on the TWP (Hoell and Funk 2013), which goes on to dictate low-level wind shear. This will be considered the normal background mechanism that generally controls deep convection. To narrow down the time domain of the second mechanism, we calculate the magnitude of SST gradient within the TWP from the NOAA Optimum Interpolation SST (OISST). Figure 12b shows a low in SST gradient from 2001-2007 that generally corresponds with the low closure period. Figure 12c shows that mean TWP SSTs during 2001-2007 were much warmer than surrounding years, with corresponding higher mean values of convective available potential energy (CAPE) during the same period. This introduces the second mechanism: a long period where anomalously high atmospheric instability favors deep isolated convection, overwhelming the usual shear mechanism.

First, the low-level shear convective mechanism is likely controlled by the dynamics of ENSO rather than TWP SST trends. This is because the TWP is always warm enough to sustain deep convection (Zhang 1993), so sources other than the TWP mean SST are more likely to explain trends in the TWP CRS. The Nino3.4 index is derived from SSTs over the central and east Pacific (Trenberth and Stepaniak 2001). Figure 13 shows deep organized CRS in the TWP as functions of Nino3.4 index and LL shear during the period where this mechanism is proposed to control convective organization. The warm ENSO SSTs that promote deep convection in the TCP are likely responsible for controlling LL shear in the TWP. As the TCP warms during ENSO warming, the pillar of convective updraft usually centered at the TWP moves eastward, disrupting the Walker circulation and enhancing zonal winds over the TWP (Huang et al. 2001; Chen et al. 2021). When this low-level shear mechanism dominates in 1987-2001 and 2007-2021, ENSO explains large CRS trends. What makes this problem complex is that during 2001-

2007, ENSO and LL shear do not explain these trends (Fig. 12a), meaning this is not the only mechanism explaining shifts in convective organization.

The convergence-instability convective mechanism arises from anomalously high TWP SSTs in comparison to the neighboring ocean SSTs during 2001-2007 (Fig 12c). This high gradient of TWP SST to surrounding basins drives circulations of rising air over the TWP that destabilizes the atmosphere and brings convergence of winds near the surface. The argument for this mechanism is that the sheer contrast between TWP SST and background ocean SST takes the reins of convection, overriding the 'usual' low-level shear mechanism that was priorly responsible for differences in deep isolated vs deep organized CRS. This may be particular to the TWP because of it being the warmest ocean pool. Convergence of water vapor is just the negative of divergence divQ, which is conveniently one of our water balance components. In Figure 7 ERA5 divQ in the TWP reaches its two most minimum values in consecutive years, 2003 and 2004. In fact, the entire period of 2001-2007 in the TWP shows divQ maintaining much lower values than in the rest of the series. Along with Fig. 12c, this confirms that the TWP generally maintained a higher state of convergence and instability throughout 2001-2007.

2001-2007 is the period that sees the hypothesized convergence-instability mechanism override the usual low-level shear mechanism in the TWP. Additionally, the residual trend exists with and without SeaFlux evaporation (Fig. 12a). It is possible that ERA5 divQ may also have some responsibility for the lack of closure in this anomalous dynamical period. A possible hypothesis is that ERA5 reanalysis responds improperly to the anomalously warm SST state of the TWP, overestimating the large convergence of water vapor, forcing the water balance residual trend downward. To explore this, the differences between ERA5 and MERRA2, SeaFlux and QuikSCAT TWP wind speeds are all compared, finding that they all agreed to have

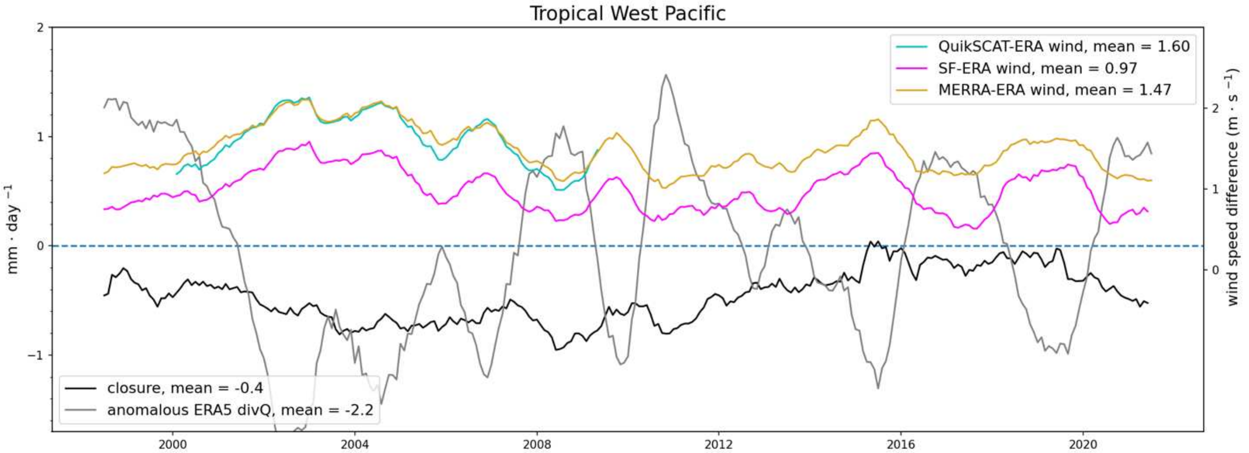

Figure 14: Three different sources of wind speed all agree that ERA has its strongest positive difference anomaly during the TWP dynamical second mechanism period of strongest convergence.

similarly shaped differences with ERA5 wind speed during the 2001-2007 convergence-instability mechanism period (Fig. 14). Interestingly, the wind speed differences across the whole time series also all anticorrelate with ERA5 divQ. These findings are not substantial enough to justify the convergence overestimation hypothesis but do leave the door open for future investigation.

3.4: The Tropical Indian Ocean

CRS in the STEI shows a clear relationship with water balance residual trend, but it cannot explain the trend according to our bias mechanism framework. Figure 15 shows that the

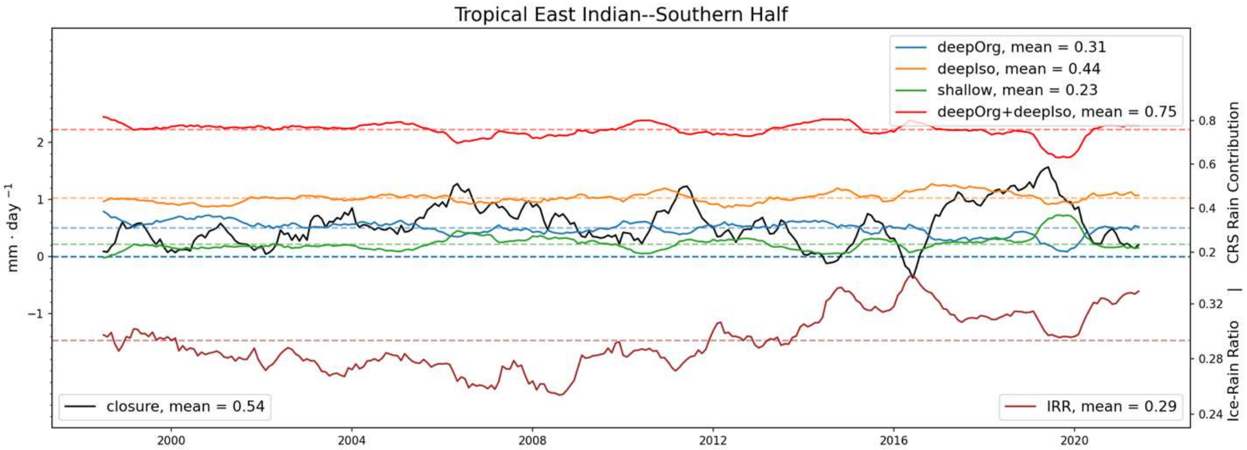

Figure 15: Rain states by themselves in the STEI are quite flat relative to the TCP and TWP, so CRS rain contributions as bias actors are not enough to explain non-closure. This basin does however have a more variable IRR than others, which serves as a causal bias actor through ice-scattering.

CRS interplaying modes are not between two dominant ones like in the TWP (isolated vs organized) and TCP (shallow vs organized), but between all three CRSs. The relationship we see in the STEI is that shallow CRS correlates with the residual trend, meaning an interplay could be formed between shallow vs deep (isolated+organized) CRS. Our bias framework dictates that isolated and shallow CRS are underestimated and thus anti-correlated with the residual trend, while deep organized CRS is overestimated and thus correlated with residual. The STEI has shallow CRS that correlates with the residual in the STEI which may seem to oppose this, but this doesn't mean our framework is compromised. Rather, these CRS trends are flatter relative to trends in the other two problem basins, with IRR fluctuations that are stronger relative to those same basins. CRS is therefore not likely to explain the lack of closure by itself, but IRR becomes a viable explanation, as it behaves differently in the STEI compared to other basins. In particular, IRR that is attributed to shallow CRS is higher than IRR of the other two CRSs (Table 2). In terms of magnitude across the tropics, IRR follows deep organized CRS (Fig. 8), but examining IRR within each basin isolates the STEI. GPCP bias should be more sensitive to IRR shifts over the STEI and TWP because average accumulations of ice in these basins is larger than in other basins (Fig. 8). Additionally, the time series of net IRR in the STEI basin has larger variations than that in other basins, and nearly double the standard deviation of net IRR in the TWP (Table 1b). IRR can be partitioned into contributions from individual CRSs, and in the other basins, all three show similar amplitudes and variations in trend to each other. In the STEI however, the large trends in the net IRR line (Fig. 15) mostly come from variations in the shallow IRR, while deep isolated and deep organized IRR remain relatively trendless with low standard deviations (Table 1b). There is no current explanation for this STEI shallow ice behavior. IRR does show some correspondences with residual trend in other basins, but it is largely a function of CRS.

However due to its differing nature in the STEI versus other basins, it is more relevant than CRS in explaining the STEI non-closure behavior from a bias perspective.

IRR can bias GPCP via ice-scattering. Larger IRR values indicate larger amounts of ice per rain amount. Larger amounts of ice above the freezing level act to mask the emission trend from rain below it in the atmosphere, causing an underestimation of rain rate, meaning it should anticorrelate with trends in the residual as a bias actor. This anticorrelation is consistent across the whole time series, but most discernable with the shorter sharper trends starting around 2014 (Fig. 15).

The Indian Ocean basin is a fundamentally different dynamical environment from the Pacific. In the context of explaining trends in bias actors, SST is less relevant than LL shear, which can be linked to both ENSO as well as the IOD. The ITCZ dictates a general northeasterly background trade-wind flow that mingles with seasonal monsoonal winds. The states of ENSO and the IOD act to shift the zone where these winds converge. The positive mode of the IOD is characterized by an anomalously cold STEI and warm TWI, and vice versa for the negative mode. Saji et al. (1999) puts forward a framework for how the IOD works, where the usual case is that the dipole is weak or negative, and the convergence zone tends to focus more around the STEI off the coast of Sumatra. When the dipole mode is positive, there are significant zonal wind anomalies, suggesting that the southeasterly trade-winds are enhanced, causing convergence further downstream in the area of the TWI.

A perspective on this LL shear relevance comes when STEI water balance residual and bias actors are viewed as 3-month smoothed functions of SST and LL shear (Fig. 16), where it becomes clear that the Southern TEI is overall more dependent on shear than SST. Additionally, the TWI shows a similar dependence on shear, bolstering the idea that this behavior is

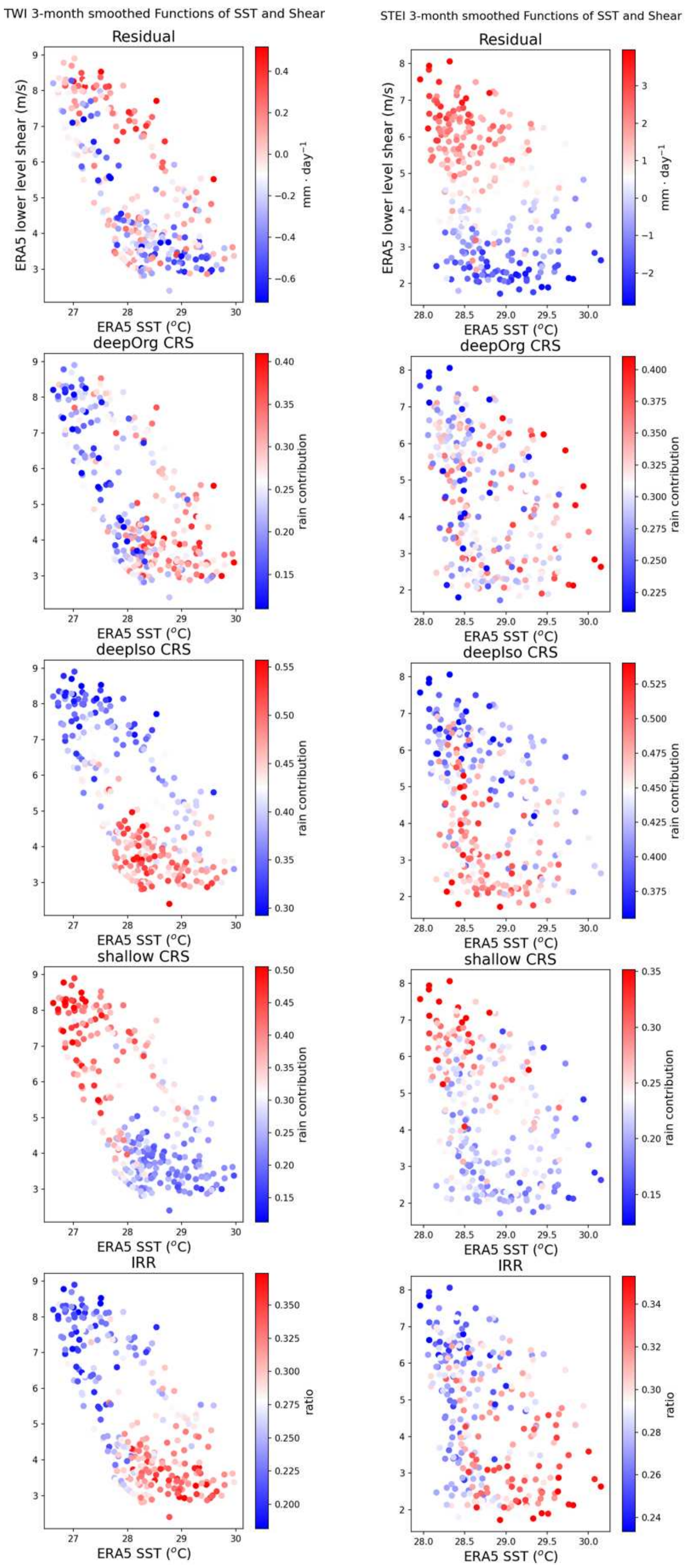

Figure 16: Water balance residual and GPCP bias actors as functions of SST and deep wind shear in the Indian Ocean basins. They are largely functions of shear. 3-smoothing filters are applied to the Pacific vs Indian basins to capture the relationships. The TWI is attached to support the argument that LL wind shear is the controlling mechanism in the whole Indian ocean.

dynamically consistent across the whole Indian Ocean basin environment. Deep isolated, shallow CRS and IRR all prove to be functions of LL shear across the STEI and TWI, while deep organized CRS sees a smaller dependence in the TWI and no dependence in the STEI. Residual trend in the STEI is dependent on trends from the bias actors and thus reflects this shear dependence, but in the TWI, there are few examples of non-closure (Fig. 2), so the residual has no shear dependence. Oddly, the shear dependences depicted in Figure 16 suggest that low-level shear promotes shallow CRS and discourages deeper convection in both the TWI and STEI. This is contrary to the notion that low-level shear promotes deeper convection, but this relationship is complex. Some shear is necessary so that a raining cold pool isn't overlaid onto a warm one, canceling the heat source, but it has been posited in that shear could also play a role in suppressing deep convective initiation (Rotunno et al. 1988; Robe and Emanuel 2001; Peters et al. 2022).

An important distinction between these STEI dynamics results and the Western Pacific is that dependences over the TWP were only discernable after applying a 12-month smoothing filter, whereas the STEI shear dependence is most clear with a 3-month filtered version of the data. If the 12-month filter is applied in the STEI, there is no discernible dependence of non-closure or bias actors on LL shear or SST. If no filter is applied in the TCP, there is only a very slight relationship between terms. This is likely because wind shear over the tropical Pacific marches to the beat of SST/ENSO, which makes dynamic contributions on multi-year timescales. The dynamical context over the Indian Ocean calls for a more complex analysis across different time scales, with the Madden-Julian Oscillation and monsoons acting on the time scale of months rather than years. These STEI results suggest that LL wind shear is the more immediate dynamic driver that enhances IRR trends and biases GPCP.

Like in the TWP, there is an example of non-GPCP bias over the STEI: the water balance residual trend over the STEI in 2016-2020. From Figure 17, we can see that an anomalously large SeaFlux evaporation trend anticorrelates with the residual trend. Evaporation in SeaFlux is mainly derived from wind speeds and SST. Investigation into these terms finds that the recorded SeaFlux SST during this period has the same signal but differs in magnitude from other SST sources like ERA5 and Smith and Reynolds' ERSST. Compared to other basins, this period of SST discrepancy is strongest in the STEI, but also weakly present in the TWI and TWP neighboring basins. This is the lowest SeaFlux SST for the STEI in the whole time series and is likely an underestimation given the better agreement of ERA5 and ERSST. This SeaFlux anomaly is the only one of its kind that has been found within the scope of this study, making it difficult to explore the source of error beyond the SST disagreement.

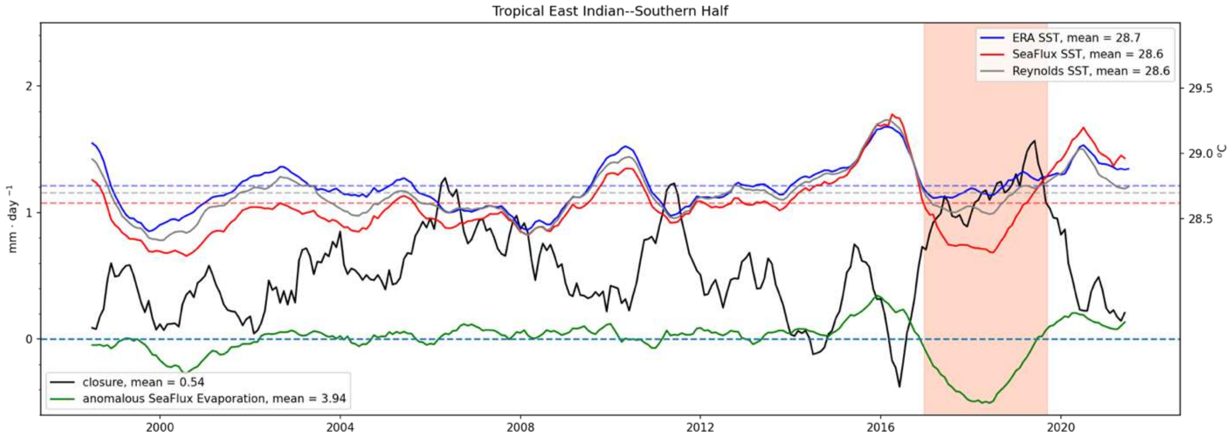

Figure 17: the largest peak in residual in the STEI is partially due to a seeming underestimation of SeaFlux SST during the highlighted 2017-2020 period. SeaFlux SST deviates heavily from ERA5 and Reynold's SST which seems to directly affect the output of SeaFlux evaporation.

3.5: Future Works

The future works motivated by this study is to both improve our understanding of tropical atmospheric dynamics while eliminating biases in remote sensing products.

This work raises questions about tropical oceanic convective processes. We don't know why shallow IRR in the STEI basin varies so much more than deep isolated or organized, ultimately controlling the trends in net IRR that biases closure. We also don't know why the LL shear seems to have an inverse relationship with deeper convection in the STEI while having a direct one in the TWP (Fig. 13; Fig. 16). Further exploration of these questions could lead to a deeper understanding of the convective-controlling mechanisms of these differing dynamical environments. Future work could include incorporating our results in model experiments to verify and expand upon our general understanding of tropical convection.

This work provides a conceptual framework for systematic errors found in precipitation observations. The authors have no access to the algorithm that output these quantities and can only show the likely source of these biases. Future work would also hopefully involve addressing these convective biases in the GPCP and other rainfall algorithms, so that scientists may have access to higher quality global rainfall data.

Relocating ocean boxes based on climatology is perhaps the simplest step to illuminating relationships. Replacing the Indian Ocean box from prior studies with two boxes based on the location of the IOD more clearly revealed large biases, revealing the relationship between non-closure, bias actors and LL shear in those regions. The same could be done for boxes over the other basins, for example with a focus on the location and movement of the ITCZ climatology in the Pacific. A separate but tangential idea would be breaking the residual term down with a seasonal analysis, which could capture the more intense phases and locations of phenomena like the IOD and ENSO that impact the bias actors.

The coincidence in the TWP of the global warming 'hiatus' period with the low-closure and SST-ENSO correlation period is perhaps the most interesting finding of this study. It indicates that large-scale variability may be connected to the frequency of occurrence of different precipitation states over the TWP.

CHAPTER 4: SUMMARY AND CONCLUSION

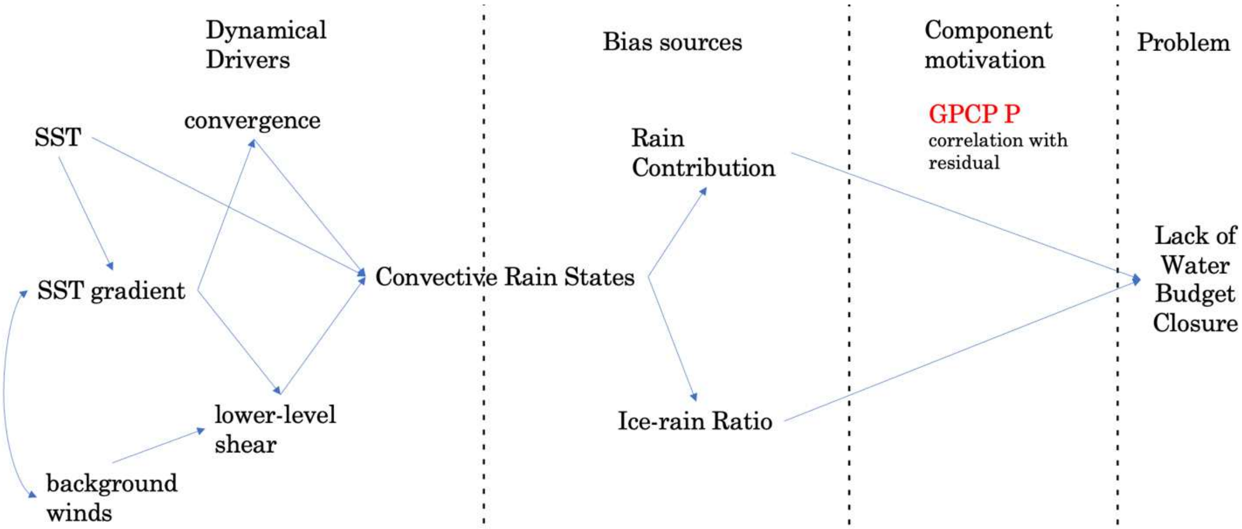

Figure 18: A map describing the main narrative put forth in this work.

Technological strides in remote sensing observations and algorithms now allow for independent hydrologic cycle data products that yield water budget results with discernable systematic biases. This work aims to answer two questions. 1) What is at the heart of water budget closure bias over Earth's tropical oceans? After determining that convective organization can be used to explain more observed water balance residuals, the second question becomes 2) what controls changes in convective organization over Earth's tropical oceans? Figure 18 is a map that summarizes the main narrative of this study's answers to these questions.

The first step was to focus on three out of the six basins that show clear long-term trends in non-closure. Through correlation and simple line-matching, we determine that out of the three water budget components that comprise the residual, GPCP precipitation is most correlated with the lack of closure, most notably in the problem basins themselves. With physical reasoning behind the CRS and ice-scattering biases, each basin is treated as a case study, and CRS rain partitions and IRR prove to be useful metrics to represent these systematic biases. The non-problem basins (TEP, TAO, TWI) all show some correspondence with CRS, but the biases are made much clearer in the problem basins (STEI, TWP, TCP). The TCP biases are a result of an interplay between shallow and deep organized CRS and the TWP between deep isolated and organized. The STEI CRS are flat in trend and thus don’t cause a CRS bias effect but rather, an anomalously active IRR behavior related to shallow CRS is found that causes an ice-scattering bias. Thus, the first question is answered, convective organization ultimately biases the GPCP water budget component over the tropical oceans through two bias actors.

The CRS and IRR say something greater about convective organization, and finding the dynamical underpinnings requires further exploration of each of the problem basins. The root of convective change in the TCP can be traced back to ENSO, where it can be shown that CRS shifts are a simple function of SST. In the STEI, the root is not as simple, as both the IOD and ENSO are known to affect large-scale wind patterns in the Indian Ocean basin. When viewed as a function of low-level wind shear rather than SST, convective shifts in the STEI as well as the TWI are illuminated. The TWP is the most complex dynamical basin but becomes explainable when separated into a time period where LL shear is the regular background mechanism that usually controls changes in convection, and convergence and instability as an anomalous mechanism that dominates when TWP SST temperatures are much warmer than their surroundings, plenty of moisture is present due to the inflow, thermal winds are higher, and LL shear is no longer needed to promote deeper convection.

Ultimately, all the arrows in the causality map eventually point to SST and background winds but getting from there to non-closure trends is not a trivial path, taking different routes that are controlled by each basin’s thermodynamic environment.

REFERENCES

Adler, R., Negri, A., Hakkarinen, I., 1991. Rain estimation from combining geosychronous IR and low-orbit microwave data. Global and Planetary Change 4, 87–92. https://doi.org/10.1016/0921-8181(91)90076-9

Adler, R., Sapiano, M., Huffman, G., Wang, J.-J., Gu, G., Bolvin, D., Chiu, L., Schneider, U., Becker, A., Nelkin, E., Xie, P., Ferraro, R., Shin, D.-B., 2018. The Global Precipitation Climatology Project (GPCP) Monthly Analysis (New Version 2.3) and a Review of 2017 Global Precipitation. Atmosphere 9, 138. https://doi.org/10.3390/atmos9040138

Adler, R.F., Gu, G., Huffman, G.J., 2012. Estimating Climatological Bias Errors for the Global Precipitation Climatology Project (GPCP). Journal of Applied Meteorology and Climatology 51, 84–99. https://doi.org/10.1175/JAMC-D-11-052.1

Adler, R.F., Huffman, G.J., Chang, A., Ferraro, R., Xie, P.-P., Janowiak, J., Rudolf, B., Schneider, U., Curtis, S., Bolvin, D., Gruber, A., Susskind, J., Arkin, P., Nelkin, E., 2003. The Version-2 Global Precipitation Climatology Project (GPCP) Monthly Precipitation Analysis (1979–Present). J. Hydrometeor 4, 1147–1167. https://doi.org/10.1175/1525-7541(2003)004<1147:TVGPCP>2.0.CO;2

Allan, R.P., Liu, C., Loeb, N.G., Palmer, M.D., Roberts, M., Smith, D., Vidale, P.-L., 2014. Changes in global net radiative imbalance 1985-2012. Geophys. Res. Lett. 41, 5588–5597. https://doi.org/10.1002/2014GL060962

Amaya, D.J., Xie, S., Miller, A.J., McPhaden, M.J., 2015. Seasonality of tropical P acific decadal trends associated with the 21st century global warming hiatus. J. Geophys. Res. Oceans 120, 6782–6798. https://doi.org/10.1002/2015JC010906

Brown, P.J., Kummerow, C.D., 2014. An Assessment of Atmospheric Water Budget Components over Tropical Oceans. Journal of Climate 27, 2054–2071. https://doi.org/10.1175/JCLI-D-13-00385.1

Chen, H., Shi, J., Jin, Y., Geng, T., Li, C., Zhang, X., 2021. Warm and Cold Episodes in Western Pacific Warm Pool and Their Linkage With ENSO Asymmetry and Diversity. JGR Oceans 126. https://doi.org/10.1029/2021JC017287

Clayson, C.A., Bogdanoff, A.S., 2013. The Effect of Diurnal Sea Surface Temperature Warming on Climatological Air–Sea Fluxes. Journal of Climate 26, 2546–2556. https://doi.org/10.1175/JCLI-D-12-00062.1

Clayson, C. A., J. B. Roberts, and A. S. Bogdanoff, 2015: The SeaFlux Turbulent Flux Dataset Version 1.0 Documentation. SeaFlux Documentation Version 1.2, 5 pp, http://seaflux.org/seaflux_data/DOCUMENTATION/SeaFluxDocumentationV12.pdf.

Dines, W.H., 2007. The heat balance of the atmosphere. Q.J.R. Meteorol. Soc. 43, 151–158. https://doi.org/10.1002/qj.49704318203

Elsaesser, G.S., Kummerow, C.D., L'Ecuyer, T.S., Takayabu, Y.N., Shige, S., 2010. Observed Self-Similarity of Precipitation Regimes over the Tropical Oceans. Journal of Climate 23, 2686–2698. https://doi.org/10.1175/2010JCLI3330.1

Fairall, C. W., E. F. Bradley, J. E. Hare, A. A. Grachev, and J. B. Edson, 2003: Bulk parameterization of air-sea fluxes: Updates and verification for the COARE algorithm. *Journal of Climate*, **16,** 571-591.

Global Modeling And Assimilation Office, Pawson, Steven, 2015. MERRA-2 tavgM_2d_flx_Nx: 2d,Monthly mean,Time-Averaged,Single-Level,Assimilation,Surface Flux Diagnostics V5.12.4. https://doi.org/10.5067/0JRLVL8YV2Y4

Graves, C.E., 1993. A Model for the Beam-filling Effect Associated with the Microwave Retrieval of Rain. J Atmos Oceanic Tech 10, 5. https://doi.org/10.1175/1520-0426(1993)010<0005:AMFTBF>2.0.CO;2

Gutenstein, M., Fennig, K., Schröder, M., Trent, T., Bakan, S., Roberts, J.B., Robertson, F.R., 2021. Intercomparison of freshwater fluxes over ocean and investigations into water budget closure. Hydrol. Earth Syst. Sci. 25, 121–146. https://doi.org/10.5194/hess-25-121-2021

Held, I.M., Soden, B.J., 2006. Robust Responses of the Hydrological Cycle to Global Warming. Journal of Climate 19, 5686–5699. https://doi.org/10.1175/JCLI3990.1

Henderson, D.S., Kummerow, C.D., Marks, D.A., 2017a. Sensitivity of Rain-Rate Estimates Related to Convective Organization: Observations from the Kwajalein, RMI, Radar. Journal of Applied Meteorology and Climatology 56, 1099–1119. https://doi.org/10.1175/JAMC-D-16-0218.1

Henderson, D.S., Kummerow, C.D., Marks, D.A., Berg, W., 2017b. A Regime-Based Evaluation of TRMM Oceanic Precipitation Biases. Journal of Atmospheric and Oceanic Technology 34, 2613–2635. https://doi.org/10.1175/JTECH-D-16-0244.1

Hersbach, H., Bell, B., Berrisford, P., Hirahara, S., Horányi, A., Muñoz-Sabater, J., Nicolas, J., Peubey, C., Radu, R., Schepers, D., Simmons, A., Soci, C., Abdalla, S., Abellan, X., Balsamo, G., Bechtold, P., Biavati, G., Bidlot, J., Bonavita, M., Chiara, G., Dahlgren, P., Dee, D., Diamantakis, M., Dragani, R., Flemming, J., Forbes, R., Fuentes, M., Geer, A., Haimberger, L., Healy, S., Hogan, R.J., Hólm, E., Janisková, M., Keeley, S., Laloyaux, P., Lopez, P., Lupu, C., Radnoti, G., Rosnay, P., Rozum, I., Vamborg, F., Villaume, S., Thépaut, J., 2020. The ERA5 global reanalysis. Q.J.R. Meteorol. Soc. 146, 1999–2049. https://doi.org/10.1002/qj.3803

Hoell, A., Funk, C., 2013. The ENSO-Related West Pacific Sea Surface Temperature Gradient. J. Climate 26, 9545–9562. https://doi.org/10.1175/JCLI-D-12-00344.1

Houze, R.A., 1994. Cloud dynamics. Academic Press, San Diego.

Huang, R., Zhang, R., Yan, B., 2001. Dynamical effect of the zonal wind anomalies over the tropical western Pacific on ENSO cycles. Sci. China Ser. D-Earth Sci. 44, 1089–1098. https://doi.org/10.1007/BF02906865

Huffman, G.J., Adler, R.F., Arkin, P., Chang, A., Ferraro, R., Gruber, A., Janowiak, J., McNab, A., Rudolf, B., Schneider, U., 1997. The Global Precipitation Climatology Project (GPCP) Combined Precipitation Dataset. Bull. Amer. Meteor. Soc. 78, 5–20. https://doi.org/10.1175/1520-0477(1997)078<0005:TGPCPG>2.0.CO;2

Huffman, G.J., A. Behrangi, D.T. Bolvin, E.J. Nelkin, 2022a. GPCP Version 3.2 Satellite-Gauge (SG) Combined Precipitation Data Set, Edited by Huffman, G.J., A. Behrangi, D.T. Bolvin, E.J. Nelkin, Greenbelt, Maryland, USA, Goddard Earth Sciences Data and Information Services Center (GES DISC),
Accessed: **[*2022/03/01*]**, doi:10.5067/MEASURES/GPCP/DATA304

Huffman, G.J., A. Behrangi, D.T. Bolvin, E.J. Nelkin, 2022b. GPCP V3.2 Release Notes. Goddard Earth Sciences Data and Information Services Center (GES DISC), https://docserver.gesdisc.eosdis.nasa.gov/public/project/MEaSUREs/GPCP/Release_Notes.GPCPV3.2.pdf

IPCC, 2021: *Climate Change 2021: The Physical Science Basis. Contribution of Working Group I to the Sixth Assessment Report of the Intergovernmental Panel on Climate Change*[Masson-Delmotte, V., P. Zhai, A. Pirani, S.L. Connors, C. Péan, S. Berger, N. Caud, Y. Chen, L. Goldfarb, M.I. Gomis, M. Huang, K. Leitzell, E. Lonnoy, J.B.R. Matthews, T.K. Maycock, T. Waterfield, O. Yelekçi, R. Yu, and B. Zhou (eds.)]. Cambridge University Press, Cambridge, United Kingdom and New York, NY, USA, In press, doi:10.1017/9781009157896.

Kao, H.-Y., Yu, J.-Y., 2009. Contrasting Eastern-Pacific and Central-Pacific Types of ENSO. Journal of Climate 22, 615–632. https://doi.org/10.1175/2008JCLI2309.1

Koeritzer, D. 2021. Trends In Regional Atmospheric Water Cycles Across Ocean Basins Diagnosed Using Multiple Products. M.S. thesis, Dept. of Atmospheric Science, Colorado State University, 73

Kummerow, C., Hong, Y., Olson, W.S., Yang, S., Adler, R.F., McCollum, J., Ferraro, R., Petty, G., Shin, D.-B., Wilheit, T.T., 2001. The Evolution of the Goddard Profiling Algorithm (GPROF) for Rainfall Estimation from Passive Microwave Sensors. J. Appl. Meteor. 40, 1801–1820. https://doi.org/10.1175/1520-0450(2001)040<1801:TEOTGP>2.0.CO;2

L'Ecuyer, T.S., Beaudoing, H.K., Rodell, M., Olson, W., Lin, B., Kato, S., Clayson, C.A., Wood, E., Sheffield, J., Adler, R., Huffman, G., Bosilovich, M., Gu, G., Robertson, F., Houser, P.R., Chambers, D., Famiglietti, J.S., Fetzer, E., Liu, W.T., Gao, X., Schlosser, C.A., Clark, E., Lettenmaier, D.P., Hilburn, K., 2015. The Observed State of the Energy Budget in the Early Twenty-First Century. Journal of Climate 28, 8319–8346. https://doi.org/10.1175/JCLI-D-14-00556.1

Liu, W.T., 1986. Statistical Relation between Monthly Mean Precipitable Water and Surface-Level Humidity over Global Oceans. Mon. Wea. Rev. 114, 1591–1602. https://doi.org/10.1175/1520-0493(1986)114<1591:SRBMMP>2.0.CO;2

NOAA National Climatic Data Center, 2018. NOAA Smith and Reynolds Extended Reconstructed Sea Surface Temperature (ERSST) Level 4 Monthly Version 5 Dataset in netCDF. https://doi.org/10.5067/ERSST-L4N50

Peixoto, J.P. and Oort, A.H. (1992) Physics of Climate. Springer-Verlag, New York, Berlin, Heidelberg.

Peters, J.M., Morrison, H., Nelson, T.C., Marquis, J.N., Mulholland, J.P., Nowotarski, C.J., 2022. The Influence of Shear on Deep Convection Initiation. Part I: Theory. Journal of the Atmospheric Sciences 79, 1669–1690. https://doi.org/10.1175/JAS-D-21-0145.1

Reynolds, R.W., Smith, T.M., Liu, C., Chelton, D.B., Casey, K.S., Schlax, M.G., 2007. Daily High-Resolution-Blended Analyses for Sea Surface Temperature. Journal of Climate 20, 5473–5496. https://doi.org/10.1175/2007JCLI1824.1

Robe, F.R., Emanuel, K.A., 2001. The Effect of Vertical Wind Shear on Radiative–Convective Equilibrium States. J. Atmos. Sci. 58, 1427–1445. https://doi.org/10.1175/1520-0469(2001)058<1427:TEOVWS>2.0.CO;2

Roberts, J.B., Clayson, C.A., Robertson, F.R., Jackson, D.L., 2010. Predicting near-surface atmospheric variables from Special Sensor Microwave/Imager using neural networks with a first-guess approach. J. Geophys. Res. 115, D19113. https://doi.org/10.1029/2009JD013099

Robertson, F.R., Roberts, J.B., Bosilovich, M.G., Bentamy, A., Clayson, C.A., Fennig, K., Schröder, M., Tomita, H., Compo, G.P., Gutenstein, M., Hersbach, H., Kobayashi, C., Ricciardulli, L., Sardeshmukh, P., Slivinski, L.C., 2020. Uncertainties in Ocean Latent Heat Flux Variations over Recent Decades in Satellite-Based Estimates and Reduced Observation Reanalyses. Journal of Climate 33, 8415–8437. https://doi.org/10.1175/JCLI-D-19-0954.1

Rodell, M., Beaudoing, H.K., L’Ecuyer, T.S., Olson, W.S., Famiglietti, J.S., Houser, P.R., Adler, R., Bosilovich, M.G., Clayson, C.A., Chambers, D., Clark, E., Fetzer, E.J., Gao, X., Gu, G., Hilburn, K., Huffman, G.J., Lettenmaier, D.P., Liu, W.T., Robertson, F.R., Schlosser, C.A., Sheffield, J., Wood, E.F., 2015. The Observed State of the Water Cycle in the Early Twenty-First Century. Journal of Climate 28, 8289–8318. https://doi.org/10.1175/JCLI-D-14-00555.1

Rotunno, R., Klemp, J.B., Weisman, M.L., 1988. A Theory for Strong, Long-Lived Squall Lines. J. Atmos. Sci. 45, 463–485. https://doi.org/10.1175/1520-0469(1988)045<0463:ATFSLL>2.0.CO;2

Saji, N.H., Goswami, B.N., Vinayachandran, P.N., Yamagata, T., 1999. A dipole mode in the tropical Indian Ocean. Nature 401, 360–363. https://doi.org/10.1038/43854

Schlosser, C.A., Houser, P.R., 2007. Assessing a Satellite-Era Perspective of the Global Water Cycle. Journal of Climate 20, 1316–1338. https://doi.org/10.1175/JCLI4057.1

SeaPAC. 2020. QuikSCAT Level 2B Ocean Wind Vectors in 12.5km Slice Composites Version 4.1. Ver. 4.1. PO.DAAC, CA, USA. Dataset accessed [2022-10-15] at https://doi.org/10.5067/QSX12-L2B41

Seto, S., 2022. Examining the Consistency of Precipitation Rate Estimates between the TRMM and GPM Ku-Band Radars. SOLA 18, 53–57. https://doi.org/10.2151/sola.2022-009

Solomon, A., Jin, F.-F., 2005. A Study of the Impact of Off-Equatorial Warm Pool SST Anomalies on ENSO Cycles. Journal of Climate 18, 274–286. https://doi.org/10.1175/JCLI-3269.1

Stephens, G.L., L'Ecuyer, T., Forbes, R., Gettelmen, A., Golaz, J.-C., Bodas-Salcedo, A., Suzuki, K., Gabriel, P., Haynes, J., 2010. Dreary state of precipitation in global models: MODEL AND OBSERVED PRECIPITATION. J. Geophys. Res. 115. https://doi.org/10.1029/2010JD014532

Stephens, G.L., Li, J., Wild, M., Clayson, C.A., Loeb, N., Kato, S., L'Ecuyer, T., Stackhouse, P.W., Lebsock, M., Andrews, T., 2012. An update on Earth's energy balance in light of the latest global observations. Nature Geosci 5, 691–696. https://doi.org/10.1038/ngeo1580

Trenberth, K.E., Fasullo, J.T., Kiehl, J., 2009. Earth's Global Energy Budget. Bull. Amer. Meteor. Soc. 90, 311–324. https://doi.org/10.1175/2008BAMS2634.1

Trenberth, K.E., Stepaniak, D.P., 2001. Indices of El Niño Evolution. J. Climate 14, 1697–1701. https://doi.org/10.1175/1520-0442(2001)014<1697:LIOENO>2.0.CO;2

Wilheit, T.T., Chang, A.T.C., Chiu, L.S., 1991. Retrieval of Monthly Rainfall Indices from Microwave Radiometric Measurements Using Probability Distribution Functions. J. Atmos. Oceanic Technol. 8, 118–136. https://doi.org/10.1175/1520-0426(1991)008<0118:ROMRIF>2.0.CO;2

Zhang, C., 1993. Large-Scale Variability of Atmospheric Deep Convection in Relation to Sea Surface Temperature in the Tropics. J. Climate 6, 1898–1913. https://doi.org/10.1175/1520-0442(1993)006<1898:LSVOAD>2.0.CO;2

Zhang, Z., Ren, B., Zheng, J., 2019. A unified complex index to characterize two types of ENSO simultaneously. Sci Rep 9, 8373. https://doi.org/10.1038/s41598-019-44617-1

APPENDIX

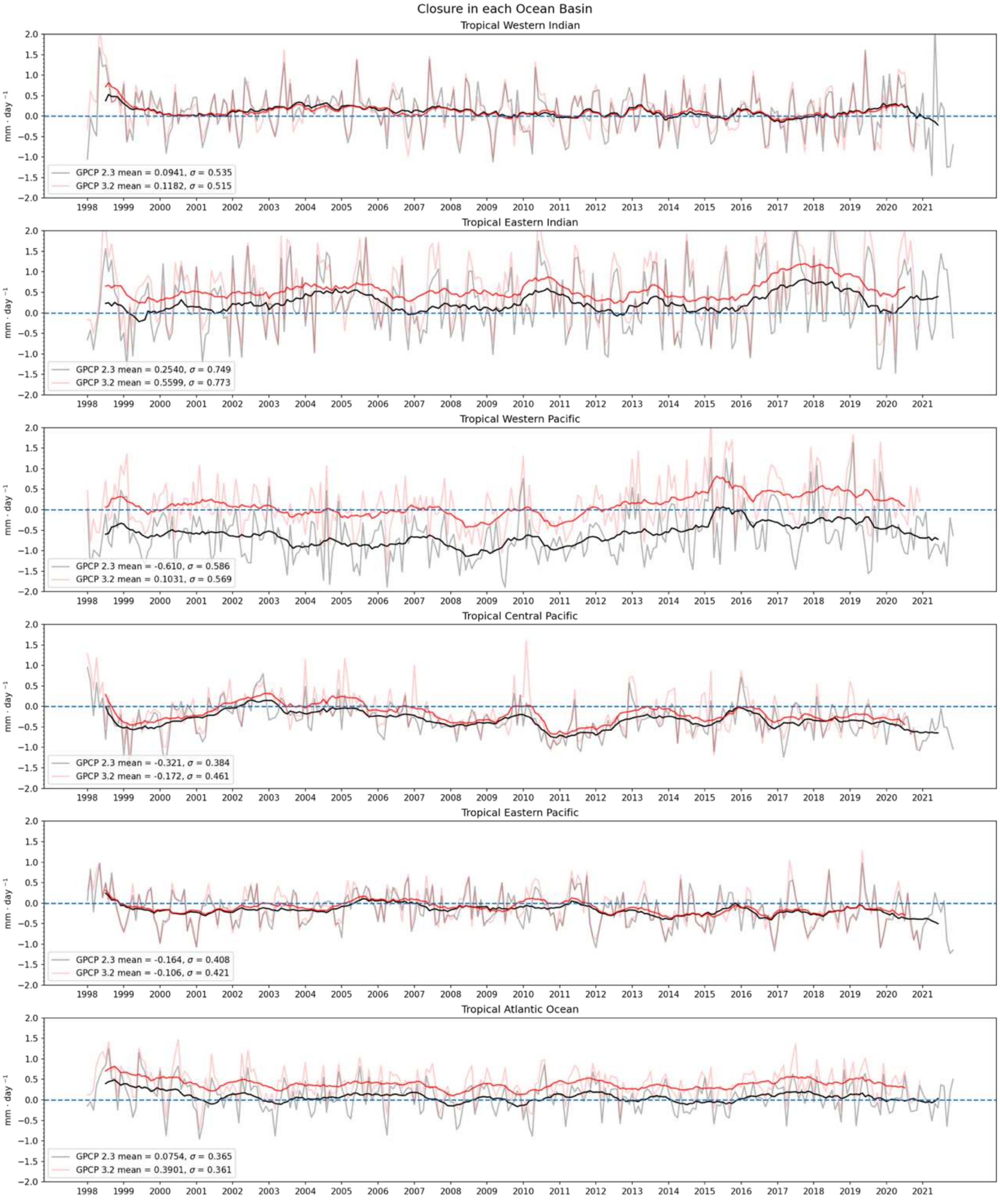

Figure S1: water balance residual from GPCP V2.3 in black versus V3.2 in red

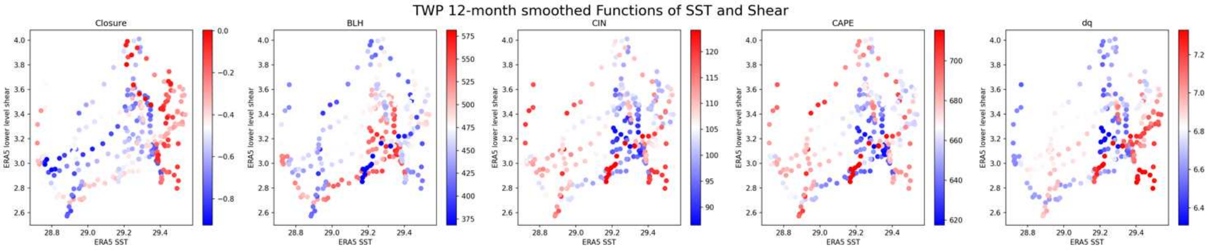

Figure S2: water balance residual plotted alongside ERA5 atmospheric stability measurements that also show a mix of strong values around the 29.3 C SST